

Resolution Limits of Time-of-Flight Mass Spectrometry with a Pulsed Source

Guangzhi Qu

Dalian, Liaoning China

Master of Science, College of William and Mary, 2009
Bachelor of Science, University of Science and Technology of China, 2007

A Dissertation presented to the Graduate Faculty
of the College of William and Mary in Candidacy for the Degree of
Doctor of Philosophy


Department of Physics

The College of William and Mary
August, 2016

APPROVAL PAGE

This Dissertation is submitted in partial fulfillment of
the requirements for the degree of

Doctor of Philosophy

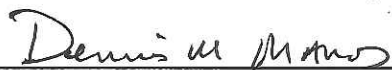


Guangzhi Qu

Approved by the Committee, August 2016



Committee Chair
Professor William Cooke, Physics
The College of William and Mary



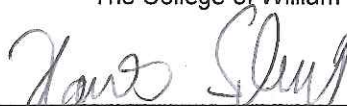
CSX Professor Dennis Manos, Physics and Applied Science
The College of William and Mary



Assistant Professor Eugeny Mikhailov, Physics
The College of William and Mary



Chancellor Professor David Armstrong, Physics
The College of William and Mary



Associate Professor Hannes Schniepp, Applied Science
The College of William and Mary

ABSTRACT PAGE

Matrix Assisted Laser Desorption/Ionization (MALDI) is a time-of-flight mass spectrometry commonly used to detect a wide mass range of biomarkers. However, MALDI requires a high laser pulse energy to create ions with a mass higher than 50,000 Daltons. That high laser energy increases the net ion production but it also degrades the instrument's mass resolution. This project uses a Room Temperature Ionization Liquid (RTIL) as a liquid matrix with a self healing surface instead of a standard crystal matrix to increase shot to shot reproducibility, enabling a systematic study of the origin of the resolution degradation. This study shows that the main source of the resolution degradation is the ionic space charge which delays the ejection of ions into the acceleration region, essentially increasing the ionization pulse time to be as long as hundreds of nanoseconds. This study includes simulation and experimental results to document this effect.

TABLE OF CONTENTS

Acknowledgements	ii
Dedications	iii
List of Figures	iv
Chapter 1. Introduction	1
Chapter 2. Theory	11
Chapter 3. Apparatus	29
Chapter 4. Non Linear Production Process and Limits on Resolution	44
Chapter 5. Simulation	61
Chapter 6. Conclusion	87
Bibliography	92
Vita	95

ACKNOWLEDGEMENTS

First and foremost, I would like to thank my advisor, Dr. William Cooke for his endless support, patient guidance and positive outlook and perseverance throughout the research. I admire the motivational optimism and excitement he shows on physics research which always inspires me with a big smile. I am so grateful for his confidence and freedom he left to me on the research. This research would not be possible if otherwise.

I would also thank Dr. Dennis Manos and Dr. Eugene Tracy contributing their brilliant suggestion and insightful questions into my research work. I have truly appreciated the group members during the years. I could not have asked for better support from such a collaborative group.

I am very fortunate to make great friends over the past years. Without your tremendous support and constant companion, I would not have so much fun during these years.

In addition, I would like to thank all staff members in physics department. Without their assistance, our graduate life would not be smooth.

Lastly, I would like to thank both of my parents. The uncertainties of pursuing degree abroad are hard to grasp. However, their confidence and faith in me supports me to finish my degree.

This Ph.D. is dedicated to my parents and my grandma

LIST OF FIGURES

1.1	Mass spectra from CIPHERGEN PBS II	2
1.2	The number of cancer death by ACS	4
1.3	Mass spectra from an NCI leukemia serum protein	7
2.1	TOF-SIMS image of prepared IMAC-Cu chip	14
2.2	Linear time of flight mass spectrometer	16
2.3	Structures of BMIM ⁺ , PF ₆ ⁻ , Imidazolium ⁺	19
2.4	Summed 100 shots spectra of copper isotopes	20
2.5	PF ₆ ⁻ peak temporal and mass resolution	22
2.6	Conventional MALDI QC spectra	23
2.7	RTIL spectra of BMIM ⁺ and PF ₆ ⁻	24
2.8	Scheme of delayed extraction	26
2.9	Conventional MALDI QC spectra in high mass range	27
3.1	Overview of vacuum chamber	31
3.2	The microchannel plate detector in Chevron mode	32
3.3	Temporal profile of ND: YAG laser pulses	35
3.4	The ionization source assembly	37
3.5	Sample holder sketch	38
3.6	Drawing of top down illumination system and stainless steel plate with a slit	39
3.7	Attenuator calibrating factor	42
3.8	Multichannel plate gain calibration	43

4.1	Positive ion from RTIL spectra	45
4.2	Integrated signal as function of laser intensity	46
4.3	BMIM ⁺ spectrum at low and high laser power	47
4.4	Heatmap of 100 laser shots at 2.5MW/cm ² laser intensity	47
4.5	Heatmap of 100 laser shots at 50MW/cm ² laser intensity	48
4.6	BMIM ⁺ single shots from figure 4.5	48
4.7	Heatmap of sorted BMIM ⁺ peaks with integral signal	49
4.8	BMIM ⁺ single shots from figure 4.8	50
4.9	Heatmap of figure 4.7 with picked fast and slow ions	52
4.10	Process to pick out fastest and slowest ion	52
4.11	Full width of BMIM ⁺ in terms of total ion intensity	53
4.12	BMIM ⁺ full width versus total signal with different detector position setup	54
4.13	Detector gain ratio calibration	56
4.14	BMIM ⁺ peak width in term of ion production with different energy	57
4.15	BMIM ⁺ peak width in term of ion production with different initial electric field	57
4.16	Heatmap of metal piece	59
4.17	BMIM ⁺ and Cr ⁺ peak width versus total ion signal	59
5.1	Time distribution of 100 ions with space charge model	63
5.2	Time distributions as ion counts increases	64
5.3	Time distributions comparison with ode45 solver and fixed	

time step solver	66
5.4 Time distribution comparison with and without image Charge	68
5.5 Time distributions of 40 thousands and 0.2 million ions	70
5.6 Ion oscillation near acceleration plate of 0.2 million ions	71
5.7 Simulation of BMIM ⁺ in 3kV/cm electric field	73
5.8 Simulation and real data conversion factor	74
5.9 Compare simulation and data with high ion count	74
5.10 Simulation of Cr ⁺ ions in 3kV/cm electric field	75
5.11 Simulation distributions with different spatial distributions	76
5.12 Simulation distributions with different launching threshold	77
5.13 Simulation distributions with different laser pulse width	78
5.14 Simulation distributions with different reservoir thickness	79
5.15 Simulation of BMIM ⁺ in 1kV/cm electric field	80
5.16 Simulation distribution of 0.4 million BMIM ⁺ at 50cm Detector	81
5.17 Time distribution of 0.4 million BMIM ⁺ vs simulation	82
5.18 Simulation of BMIM ⁺ at 10cm and 50cm detector	83
5.19 CPU and GPU architecture comparison	85
5.20 Slice model simulation of 400 thousands BMIM ⁺	86
5.21 Comparison between ion reservoir model and slice model	87

Chapter 1

Introduction

The principles of time of flight (TOF) mass spectrometry (MS) have been established for decades [1, 2, 3]. But after the first demonstration of a laser in 1960 by Theodore H. Maiman, the TOF-MS technique underwent rapid development. This was particularly true after Karas, Bachmann and Hillenkamp introduced Matrix Assisted Laser Desorption (MALDI) in 1985 [4], which provided a soft ionization mechanism so that time of flight mass spectrometry could detect biomarkers in a relatively wide mass range [5]. However, in order to see the highest mass ions, one typically uses a high laser power, which degrades the resolution of the time of flight mass spectrometer. Even narrow, atomic lines show a broadening at high laser powers, which has been interpreted as being due to a wide spread of initial velocities. Figure 1.1 displays two spectra produced by different laser powers. The spectrum is from the Quality Control (QC) data of a

Leukemia study organized by John Semmes of the Eastern Virginia Medical School. The net ion production grows as laser power increases, but the resolution of the spectra decreases. The peaks grow broader and shift towards later times. The resolution decrease obscures some of the smaller biomarkers that are adjacent to dominant peaks, such as those marked by green circles. We observe the same phenomena in our experiments. This thesis demonstrates that this resolution decrease is not due to velocity spread, but that the large ion cloud creates a space charge that prevents ions from entering the accelerating field. Thus, the broadened lines are due to a spread of times that the ions enter the accelerating region, not a spread of initial velocities.

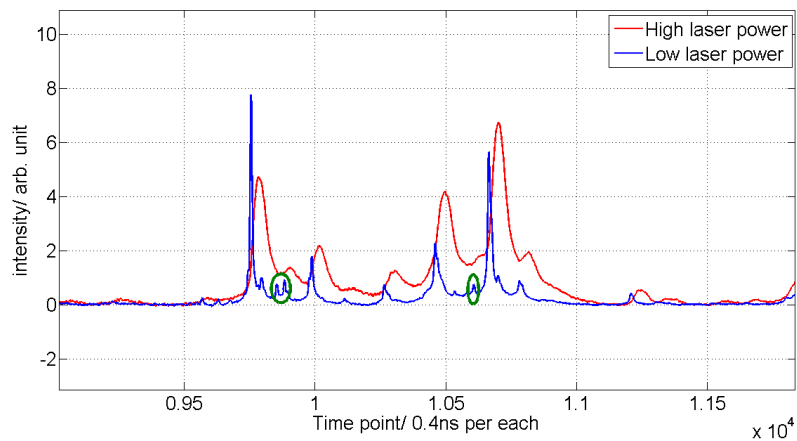


Figure 1.1 Typical mass spectra at high and low laser power using a CIPHERgen PBS II instrument to analyze QC blood serum.

1.1 Motivation

1.1.1 Early Cancer Diagnose

Cancer has been a major social health problem over recent years in the United States and all over the world. It is expected to soon be the leading disease causing premature death, surpassing heart disease. Cancer Facts & Figure 2015 (American Cancer Society) [6] estimates annual rates in the United States of 1,658,370 newly diagnosed cancer cases diagnosed and 589,430 cancer deaths.

Early diagnosis can be crucial in the treatment and control of cancer. Although conventional diagnosis strategies have improved detection, the sensitivity and specificity of these methods are still not decisive in the early stages. In most cases, a clinician analyzes a sample tissue from patients, using an optical microscope. But, often this biopsy process happens in a relatively late stage. Many cancer cases are not diagnosed and treated until abnormal cancer cells have had time to spread out to invade the surrounding tissue. Treatment is much more difficult once a tumor spreads from its original site. Cancer detection at early stage, especially at a premalignant stage would likely decrease the death rate and improve treatment strategies.

Total Number of Cancer Deaths Averted from 1991 to 2011 in Men and 1992 to 2011 in Women

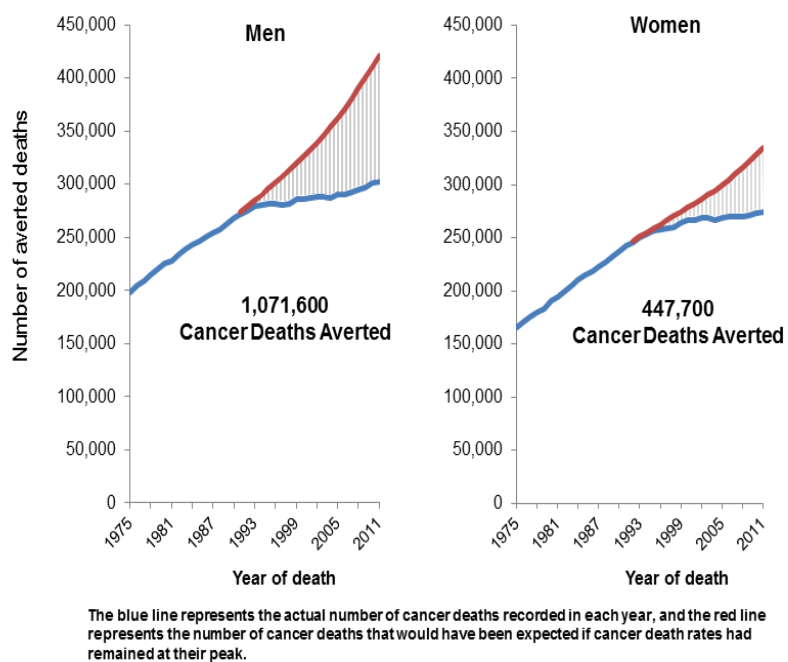


Figure 1.2 The number of cancer deaths for men (1991 to 2011) and women (1992 to 2011) as reported by the American Cancer Society

1.1.2 Proteomics and Biomarkers

Although many diseases have now been determined to be the result of defective genes, the expression of that and most other diseases occurs when new or different proteins are produced, either by the defective genes, or by the other disease agents. Thus, the proteins in a person encode, in a very complex way, the current state of that person's health. However, there are many thousands of different proteins in any person at any time. The study of these proteins, called proteomics, began at the end of last century [7, 8]. Most proteins are normal products of life, but some researchers began an attempt to identify specific proteins that represent the presence of various cancers [9, 10]. The Semmes group at the Eastern Virginia Medical School (EVMS) began a series of experiments to find proteins indicative of breast and prostate cancer in blood serum. This began with a survey of as broad mass range of proteins as possible using MALDI to ionize the proteins, and time-of-flight to identify their charge to mass ratio. Due to the complexity and variability of biological material, mass spectrometry is a powerful tool to detect and identify proteins and peptides in a broad mass range. A protein that correlates with the presence or absence of a disease is called a biomarker, such

a biomarker, if it is detected when the disease is in its early stages, could significantly improve the planned treatment of that cancer. Both single biomarkers and patterns of biomarkers can be applied to detection [10, 11, 12]. Biomarker pattern analysis as an identification of disease [13, 14] has been proven to be more effective than any individual biomarker. Correlations among abundant biomarkers require high sensitivity and high accuracy. Time of flight mass spectrometry is suited for this need by detecting all of the ionized species from a sample simultaneously. The output data from TOF-MS is a plot of signal intensity versus flight time, and is referred to as a mass spectrum. The flight time can be converted into a mass to charge ratio to identify specific biological molecules while the signal intensity (the number of ions striking detector) represents the quantity of those molecules (although different molecules can have different ionization likelihoods). Figure 1.3 is a portion of a typical mass spectra, where each peak in the spectrum represents the number of simply charged ions presumed to the peak at a particular mass.

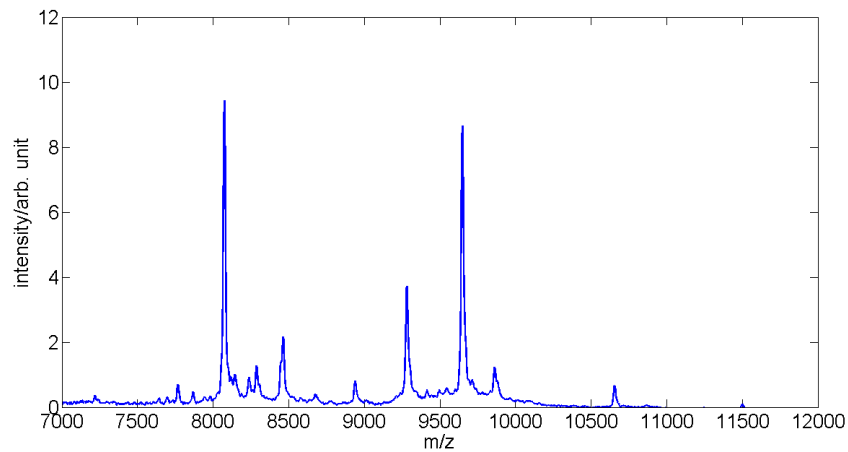


Figure 1.3 A mass spectra from 7,000 to 10,000 Da from an NCI leukemia serum protein profiling study. The patient serum samples from Quality Control (QC) pooled sera, purified and robotically spotted on IMAC-Cu affinity capture surfaces. The data were acquired over the range of 2-200kDa using a CIPHERgen PBS II instrument.

1.1.3 MALDI/SELDI

Matrix Assisted Laser Desorption/Ionization (MALDI) is a prominent MS technique with high accuracy and sensitivity to detect peptides and proteins [15, 16]. Karas, Bachmann and Hillenkamp first introduced the matrix assisted technique in 1985, and this initiated laser desorption for biophysics [4]. The first sample was a laser absorbing molecule mixed with alanine and dried on a 5-10 μm thick aluminum plate. Desorption of alanine molecules with presence of matrix molecules was observed with a laser irradiance ten times smaller than that needed to produce

peaks from alanine molecules only [4]. Contrary to previous desorption research looking for an efficiency dependence on the laser wavelength, Karas suggested controlling the energy deposition at a fixed wavelength.

Unlike standard laser desorption ionization, MALDI is a soft ionization technique that minimizes the fragmentation of large mass proteins [15, 16, 17]. MALDI TOF MS is good at detecting a broad mass range of proteins up to hundreds of kDa with high sensitivity. A sample mixed with a matrix material dries into a crystalline form. The chemical matrix material is selected to absorb the laser light as an Energy Absorbing Matrix (EAM). A single laser pulse vaporizes and ionizes a portion of the matrix carrying with it any biological material encased within it.

Thus, the desorbed ion plume contains both matrix molecules and analyte material. Within the hot and dense plume, the analyte material can also be ionized by collisions with the matrix molecules. A time of flight mass spectrometer analyzes the ionized plume by accelerating it through a fixed potential, and then timing the arrival of the ions downstream. To the extent that all the molecules are accelerated to the same energy, the heavy ions will move slower, and arrive at the detector last.

One crucial drawback of conventional MALDI is the irregular crystal surface where the local electric field is distorted near the surface. In

addition, the MALDI sample surface degradation limits its function since each laser shot removes a portion of the matrix, generating a different configuration of irregular edges. Simple MALDI matrix with standards RTILs by Armstrong, et al., achieved little success.

Improvements with mixes of classical MALDI and RTILs were made by Zabet-Moghaddam, et al. The breakthrough of RTILs usage in MALDI technique was from Armstrong et al., building novel ionic liquids known as Ionic Liquid Matrices (ILMs) by mixing the base from ionic liquids with acidic MALDI matrix [17, 18, 20, 21]. Desorption from Room Temperature Ionic Liquid (RTIL) presented in this thesis overcomes the drawback of conventional MALDI by replacing the solid MALDI matrix surface with self healing liquid surface to remove irregularities as well as provide the sample with much longer life time.

Another common soft ionization technique is electrospray ionization (ESI). Unlike MALDI, ESI produces ions by applying electric field to transfer ions from aqueous solution into gaseous phase before mass spectrometric analysis [22, 23, 24]. This makes ESI inappropriate for tissue imaging which is one of advanced uses of MALDI. Moreover, ESI often routinely attaches multiple numbers of electrons to molecules to ionize them, and this complicates the spectra.

1.2 Dissertation Outline

This dissertation has six chapters. This chapter provides an overview of current research work and a brief introduction of the terminology used in this thesis, including proteomics, biomarkers, conventional MALDI and RTIL. Chapter two introduces the theory and methodology of conventional MALDI and SELDI. Chapter two also provides details on Room Temperature Ionic Liquids. Chapter three describes the apparatus and the procedures used in the experiments. This includes a description of the vacuum system, the laser system and the data acquisition and presents some data produced from our time of flight mass spectrometer. Chapter four discusses resolution of spectrum from our system. Ion production varies dramatically shot by shot. The resolution decreases with stronger ion signal. We explore the reason for the resolution degradation which we show to be due to space charge instead of the initial ejection energy distribution. Chapter 5 presents the simulation that reproduces the resolution degradation with ion desorption signal growth to provide a proper model to explain the phenomenon. The last chapter draws conclusions from the experiment and the simulation work.

Chapter 2

Theory

This dissertation uses an ionization/desorption method that is very similar to conventional MALDI. Consequently, this chapter will discuss the theory and experiment methodology of convention MALDI and SELDI. Room temperature ionic liquids will also be introduced.

2.1 Conventional MALDI and SELDI

2.1.1 MALDI and SELDI

Matrix Assisted Laser Desorption Ionization (MALDI) is a versatile soft ionization technique used in the analysis of biological samples, especially peptides and proteins. Typically, samples are mixed with organic matrix compounds that are extremely efficient absorbers at specific wavelengths [25, 26]. The analyte molecules are typically

much less efficient in absorbing the laser energy, so they do not directly ionize or fragment. The matrix ionization is believed to be due to multiphoton absorption [25], although other models, *i.e.* energy pooling, excited state proton transfer, and thermal ionization, have been proposed to explain the MALDI process. In a multiphoton ionization process, the matrix molecules are directly ionized as an electron escapes from a neutral matrix molecule after absorbing n photons in equation 2.1.



Collisional reactions between matrix ions and matrix neutrals in the gas phase then create protonated matrix ions, as in equation 2.2.

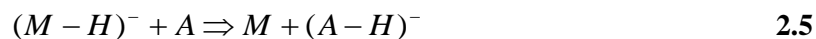


Pronated matrix ions then donate H^+ during collisions with the analyte molecules where A stands for the analyte (Eq. 2.3).



A similar process can also form negative analyte ions. A deprotonated matrix excited molecule captures a free electron becoming a deprotonated matrix ion (Eq. 2.4). Then the deprotonated matrix ion can turn deprotonate analyte (Eq. 2.5)





Another primary mechanism to form analyte anions is dissociative electron capture. (Eq. 2.6)



The MALDI processes discussed above happen within the hot MALDI plume in a short time frame after the laser pulse scattering. The plume will maintain a high molecule density for only a few nanoseconds, giving a short start time for the time of flight measurement. As a result of the phase transition from solid to gas, the MALDI ions within the hot plume typically reach velocities around 1000 m/s.

Surface Enhanced Laser Desorption Ionization (SELDI) is a variation of the soft ionization technique similar to MALDI [27]. SELDI uses a binding material on the surface of the substrate that binds specific proteins while allowing other to be washed off before the matrix is applied. This concentration step can reduce some of the common, overly abundant proteins that otherwise would dominate a spectrum. The final step is still the application of the matrix compound that crystallizes with the sample proteins and peptides. Both MALDI and SELDI have complicated surface structures. Figure 2.1 is an optical image (acquired by a PHI Thrift III, Time-Of-Flight Secondary Ion Mass Spectrometry, TOF-SIMS, instrument, courtesy of Dasha Malyarenko)

of a prepared SELDI IMAC-Cu chip sample containing pooled blood serum and matrix material that has been prepared for use on a CIPHERGEN PBS-2 SELDI-TOF instrument. Both MALDI and SELDI have shown limited reproducibility due to all of these preparations steps and the physical surface structure damage with increased laser shot counts.

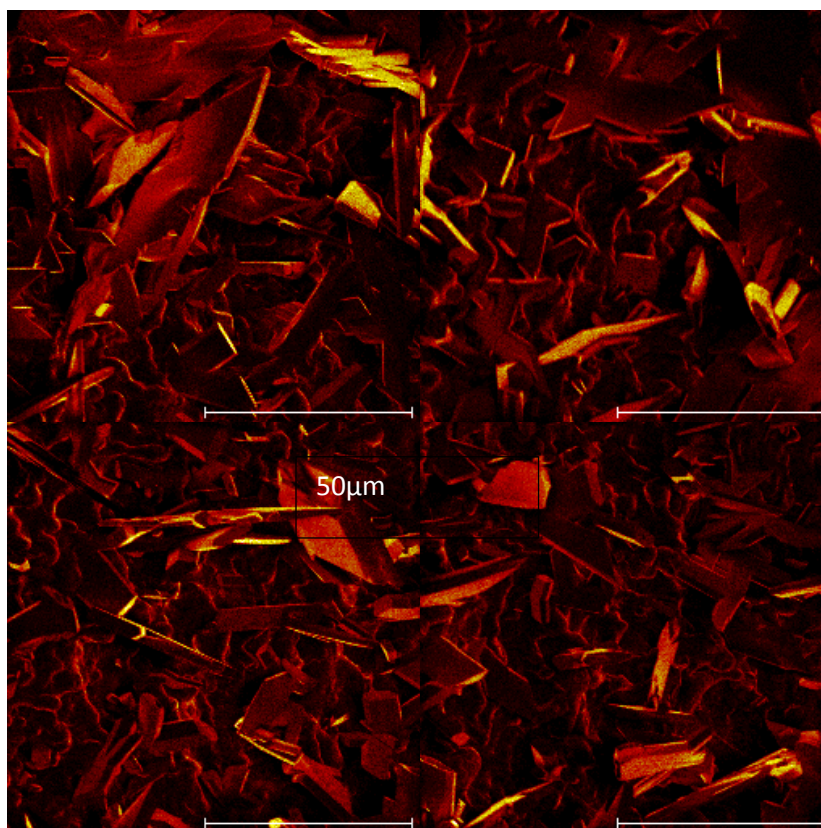


Figure 2.1 Time of Flight Secondary Ion Mass Spectrometry (TOF-SIMS) image of a prepared SELDI IMAC-Cu sample chip. The crystalline sample surface is rough and irregular. The sample pictured consists of pooled blood serum and a MALDI matrix. Both samples have similar surface structures after matrix application. Such structures and features limit resolution and reproducibility of TOF spectra.

2.1.2 Time of Flight of Mass Spectrometry

Time of Flight Mass Spectrometry (TOF-MS) was one of the earliest mass spectrometry techniques, originally introduced in the late 1940's [1, 2]. A TOF mass spectrometer creates ions in a short burst, accelerates the ions through a fixed voltage and then measures the time it takes ions to travel through a long, field-free distance. If all the ions start at the same time and have the same energy, then their arrival times will be proportional to the square root of their mass to charge ratio. For most TOF mass spectrometers, each ion travels the same distance in the direction of the acceleration field, so the major limitations to TOF resolution are the time it takes to create the ion burst and the energy spread of the initial ions before they are accelerated. Figure 2.2 shows a typical schematic for a linear TOF mass spectrometer.

Consider an ion of mass m , charge q , and initial velocity v_0 (in the acceleration direction) created at time t_0 and the accelerated through a voltage V applied to plates separated by a distance d , followed by a field-free region of length L . The arrival time at the detector (Eq. 2.7) will be

$$T = t_0 + \frac{L + 2d}{\sqrt{\frac{2qV}{m} + v_0^2}} \approx t_0 + \sqrt{\frac{m}{q}} \left(\frac{L + 2d}{\sqrt{2V}} \right) \left(1 - \left(\frac{v_0^2}{4V} \right) \frac{m}{q} \right) \quad 2.7$$

When all ions are created at same time, and the initial velocity is small, then the ration q/m can be precisely calculated, although the scale factor $\left(\frac{L + 2d}{\sqrt{2V}} \right)$ is more commonly calibrated by measuring the arrival time of a known ion.

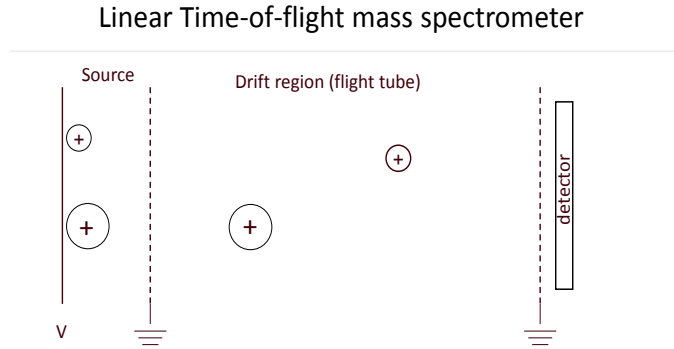


Figure 2.2 In linear TOF-MS, ions are formed by a laser pulse, and accelerated through a constant potential in the source region. Having the same energy, lighter ions reach the detector faster than heavier ones.

There are some other commonly used mass spectrometry methods which could also obtain high resolution mass spectrum. Quadrupole filter is one of these widely used mass analyzer [28]. It consists of four cylindrical rods which are parallel to each other, separating ions in the oscillating electric field. Quadrupole filter typically depends on other continuous ionization methods such as electron-impact which is not

particularly well suited for pulsed work. They have been used in tandem with a TOF systems, where the TOF system acts as a pre-filter, allowing the high resolution quadrupole system to separate fine details. Other high resolution techniques, like ion traps[29, 30], are similar to quadrupole filters in not producing the wide range of q/m values necessary for a wide survey for a small sample of analytes, such as is considered here.

2.2 Room Temperature Ionic Liquids

Similar to conventional solid state salt, room temperature ionic liquids (RTIL) are comprised of positive and negative ions; however, RTIL is in a liquid phase at room temperature as described by the name.

Although a liquid, RTIL has the unusual property of a very low vapor pressure, making it appropriate for use in a vacuum chamber [31]. As an example, a small sample of RTIL in our experiment situated in our copper sample holder lasts months with no evidence of evaporation while the vacuum is maintained at 10^{-9} torr. This extremely low vapor pressure stimulated early interest in RTIL research in chemistry as a new class of non-volatile solvents, although many are toxic. The extremely low vapor pressure of RTIL in physics guarantees the stability for use under high vacuum, a property more typical of solids [32, 33, 34]. An RTIL ionization source has a few primary advantages.

First, the liquid surface of RTIL provides a smooth, repeatable experimental surface. Conventional MALDI surfaces are crystalline insulators with inhomogeneous initial electric fields that change after each laser pulse. An inhomogeneous electric field surface distribution degrades the temporal resolution of the MALDI technique. Secondly, the liquid RTIL surface refills the evaporated material, so the surface never changes. Finally, in contrast to conventional MALDI where ionization builds from collisions of matrix ions and neutrals, RTIL is a precharged species that can ionize the analyte through potential ionization or gentle attachment of an RTIL primary cation or anion to the analyte molecule.

In our experiment, we use one of the most common RTILs: 1-butyl, 3-methylimidazolium hexafluorophosphate, $\text{BMIM}^+ \text{PF}_6^-$. The structure and mass are shown in Fig. 2.3. $\text{BMIM}^+ \text{PF}_6^-$ has been well studied and is commercially available from reliable chemical companies (Sigma-Aldrich, Fluka #70956, Switzerland). Beyond this, $\text{BMIM}^+ \text{PF}_6^-$ has the common properties mentioned above, liquid at room temperature, low vapor pressure and ionic composition. In our experiments, we have observed that the negative ion, i.e. PF_6^- is stable throughout its travel to the detector, while the BMIM^+ ion fragments, producing Imidazolium⁺, during its free-flight. This fragmentation is greater with higher laser power. $[\text{BMIM}^+][\text{PF}_6^-]$ is transparent to visible light and

does not absorb at the wavelength of our Nd:YAG 532nm laser. However, at high laser intensities, multiphoton absorption does produce a strong ionization desorption spectrum. Similarly, metal ions, e.g. chromium ions, also produce an ionization spectrum at similar laser intensities.

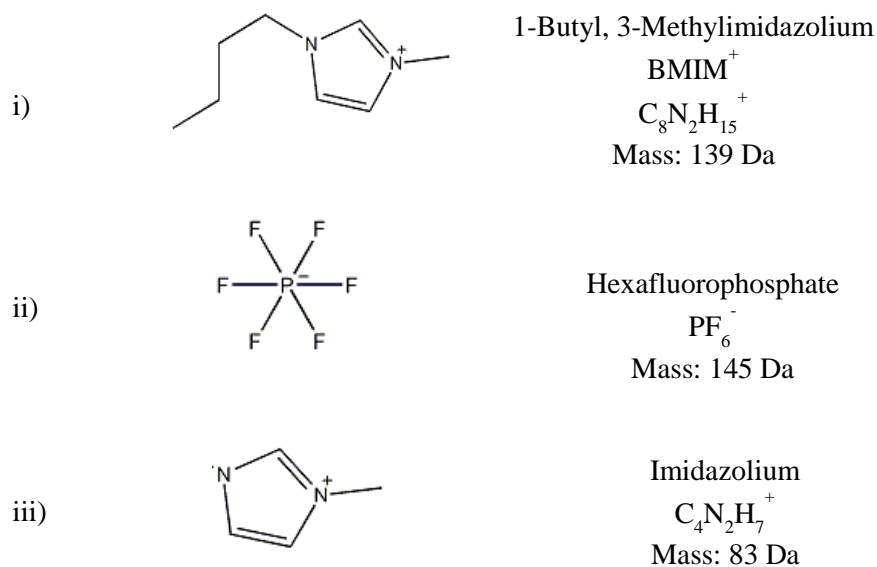


Figure 2.3 Structures of (i) BMIM⁺, (ii) PF₆⁻, and (iii) Imidazolium⁺, the primary fragment of BMIM⁺. These three ions are the most abundant species present in our desorption spectra, in addition to any metal ions. Aside from Imidazolium, there is another remnant BMIM fragment (56 Da) present in desorption spectra, though it is less stable, and frequently fragments further.

2.3 Resolution

2.3.1 Definition

In time of flight mass spectrometry resolution is the ability to identify ions of different ion species in a single spectra. Figure 2.4 displays copper isotopes from our laser desorption system to illustrate mass peaks that are well resolved. These mass spectra use a conversion from the arrival time of the ions to the ions charge to mass ratio, which is a linear relationship over small mass ranges. So, one can use either time spectra or mass spectra to illustrate resolution. In this dissertation we will focus on temporal resolution which relates more closely to physical process studied.

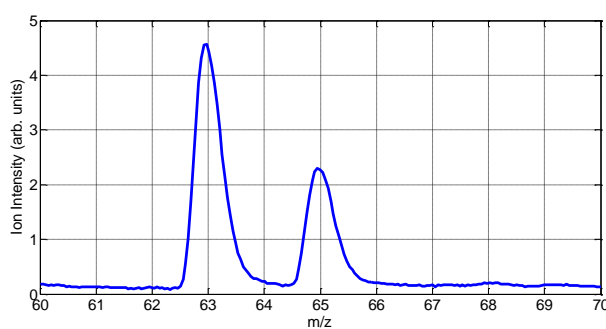


Figure 2.4 summed 100 shots spectra, displaying copper isotope peaks

The temporal resolution of a peak in a spectrum defined as the ratio of its central arrival time t to the spread of arrival times, Δt . We will define Δt to be the full width at half maximum of the peak (Eq. 2.8).

$$resolution = \frac{t}{\Delta t} \quad 2.8$$

For time of flight mass spectrometry, the mass resolution and the temporal resolution are simply related. Because the kinetic energy of the ions are fixed by the acceleration, all the ions will have the same value of mv^2 . But, the ion speed and arrival time are inversely related.

$$vt = L \quad 2.9$$

$$vdt + t dv = 0 \quad 2.10$$

$$\frac{v}{dv} = -\frac{t}{dt} \quad 2.11$$

so the time resolution is the same as the velocity resolution. Using this, with the constant kinetic energy, we find:

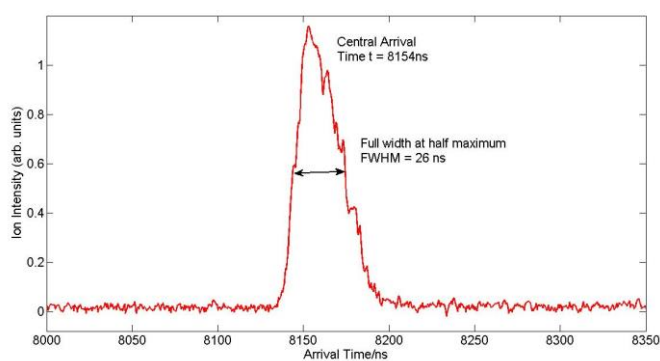
$$qV = \frac{1}{2}mv^2 \Rightarrow v^2 dm + 2mvdv = 0 \quad 2.12$$

$$\frac{v}{dv} = -\frac{2m}{dm} \quad 2.13$$

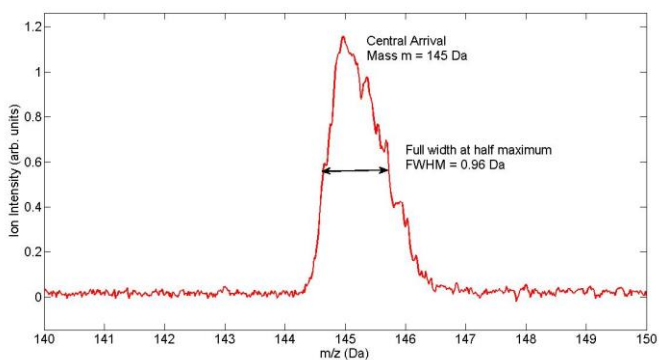
The relation between temporal and mass resolution is thus:

$$\frac{m}{\Delta m} = \frac{t}{2\Delta t} \quad 2.14$$

Figures 2.5a) & b) display PF_6 negative ion peak temporal and mass resolution which are consistent with Eq. 2.14.



a)



b)

Figure 2.5 Data showing the arrival time of a negative PF_6 ion after traveling 0.5 m with an energy of 3KeV in the top graph, and the m/z values in the bottom graph. The temporal resolution is around 310. Whereas the mass resolution, at 150, is half as large.

2.3.2 MALDI resolution

Conventional MALDI has fundamental limits on its intrinsic resolution. The nature of a hot, exploding collisional plume after the desorption process broadens the initial energies to degrade the resolution. A low mass spectra produced by conventional MALDI (20kV energy) in figure 2.6 shows this degradation. Within the same mass range, our laser

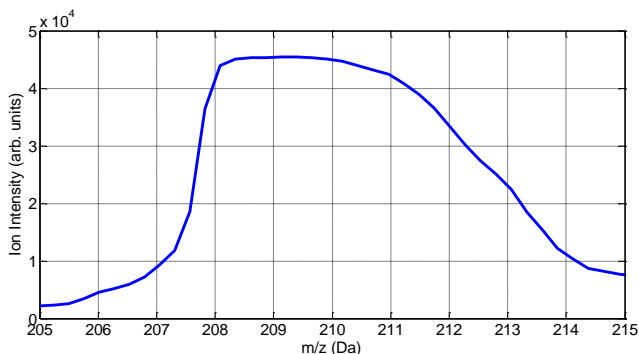


Figure 2.6 A conventional MALDI, quality control spectra, taken at EVMS using a Ciphergen PBS2 instrument, displaying one of the better resolved peaks within the low mass range. This peak suffers from poor resolution and a distorted peak shape.

desorption spectra, Fig. 2.7, of an RTIL ionization source offers better resolution and peak shape. This improvement in resolution is not an artificial effect of the acceleration voltage setting, as conventional MALDI uses much higher voltage than our RTIL desorption.

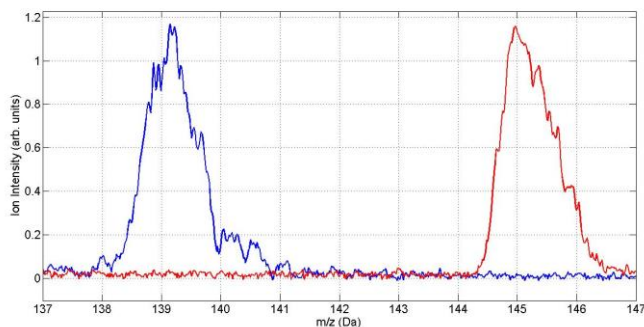


Figure 2.7 RTIL desorption, summed 100 shot spectra, displaying both positive (blue) and negative (red) spectra over the same mass range. BMIM^+ (139.2 Da) and PF_6^- (145.0 Da) peaks are clearly present with a mass resolution of ~ 150 . The shoulder on the right side of the BMIM^+ peak is indicative of its isotopic structure. PF_6^- is without isotopes.

To achieve higher resolution for high mass ion species, MALDI applies a variety of techniques to enhance the spectral resolution, such as a high acceleration voltage, delayed extraction, and reflection operation mode.

Using a high acceleration voltage intrinsically increases the resolution, and also reduces the resolution degradation affiliated with the initial energy spread:

$$\frac{m}{\Delta m} = \frac{E_{final}}{\Delta E_{final}} = \frac{qV + E_i}{\Delta E} \cong \frac{qV}{\Delta E} \quad 2.15$$

Equation 2.15 shows that the mass resolution increases for higher acceleration voltages. MALDI typically uses high acceleration voltages

of 10 to 20KV, whereas we restricted ours to 1 to 3KV. High acceleration voltages produce very fast ions which then require a long free-flight travel region in order to make the arrival time much longer than the creation time. A 2 m flight region is not uncommon for a TOF-MS apparatus, and some also use a reflectron to make the ions travel twice through the free-flight region. We kept our apparatus simple (no reflectron) and reasonably short (<0.5 m), and this necessitated that we use a low acceleration voltage.

Laser desorption typically produces a plume with an average ejection velocity of 800-1000 m/s, and the velocity spread is a significant fraction of that. Delayed extraction is probably the most common arrival time reduction technique [35]. If one delays applying the extraction voltage for a short time, the faster ions will move farther away from the sample, so that when the extraction voltage is applied, the fast ions will travel through a smaller voltage drop. Thus, by the end of the acceleration region, the initially slow ions will have gained more energy and will then have a more similar velocity to the initially fast ions. This technique requires careful tuning of the delay time, and it only works for a band of ions centered around one value of q/m .

Initially fast ions with a mass lower than the target mass will have moved too far and will end up with less energy than the slow ions of the same mass. Consequently, delayed time extraction only narrows

the arrival time for ions within a mass-focusing range (which is determined by the delay time). Figure 2.8 illustrates this technique.

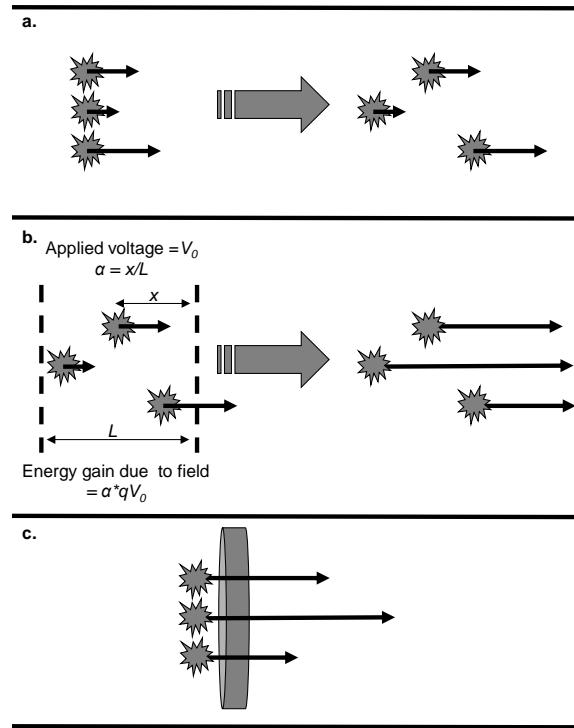


Figure 2.8 Delayed Extraction Schematic. a. Same mass ions with different initial velocities are allowed to separate spatially, before the application of an extraction field. b. Extraction field applied such that each ion experiences a different position based acceleration. c. Same mass ions, each with different final velocities, arrive simultaneously at detector.

The other common resolution technique is to use a reflectron. Not only does this increase the effective length that the ions travel, but the electrostatic mirror that reflects the ion will also decrease the initial energy spread [36]. More energetic ions travel a longer path by penetrating deeper into the mirror than slow ions. The detector then

collects all the ions at the focal point of electrostatic mirror where all the arrival times of one species match. A final common approach to enhance the resolution is to use tandem TOF-MS, which consists of sequential acceleration and free flight apparatuses, taking only a small time slice from the first spectrometer as input to the second one. Any of these TOF-MS methods that depend on a short creation burst suffer a loss of resolution at high production rates. When the signals in a single burst are large, then isotopically selected ions show broadening of the arrival times. This dissertation explores the reasons for this decrease in time resolution.

MALDI produces decent resolution time of flight spectra with the incorporated techniques mentioned, specifically at high mass range. Blood serum peptide of mass 7777 Da in figure 2.9 reveals excellent resolution from MALDI with incorporation of several of these enhancing techniques. Our laser desorption from room temperature ionic liquid is

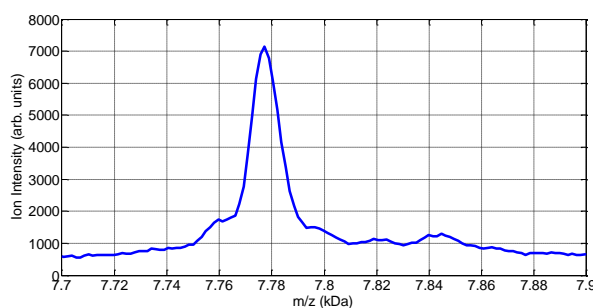


Figure 2.9 Conventional MALDI quality control spectra, in the high mass range, using delayed extraction, high acceleration voltage. Peptide of mass 7777 Da with a good mass resolution of ~600.

competitive with conventional MALDI without applying any resolution enhancing techniques discussed.

Chapter 3

Apparatus

This chapter describes components of our experimental apparatus. All the ionization and detection occurs in a vacuum chamber. The detection system, consisting of microchannel plates and a collection plate, sits in the top region of the vacuum chamber and provides highly efficient ion detection. Outside the chamber, a laser system generates laser pulses that initiate the ion desorption process. A top-down illumination reflection system focuses the laser beam onto the surface of the sample holder inside the vacuum chamber. The data acquisition system stores and analyzes the experimental data. The following sections describe the details of each component.

3.1 Vacuum System

The vacuum chamber is constructed from standard stainless steel components, including a 6 way cross, an 8.5" long full nipple and an octagonal source chamber, all connected via 6" Conflat flanges. The octagonal source chamber has eight 2.75" Conflat port windows along the edge of a ring with a 6" Conflat flange port window below. Figure 3.1 shows the layout of the entire chamber, vertically oriented with the sample at bottom while allowing laser access from below. The free-flight region is ~0.5 meter, consisting of a portion of the 6-way cross and the full nipple flange. The sample assembly sits inside the octagonal chamber at the bottom adjacent to the windows and the high voltage feed-through ports.

The entire chamber assembly is mounted in a customized Unistrut structure, sitting securely on an 8'x4' optical table. The vacuum pumps are mounted from an elbow flange on the central 6-way cross. The pressure in the chamber is maintained at 10^{-9} torr by a Leybold Turbovac 152 turbomolecular pump (145 l/s) in combination with a Varian SD200 Rotary Vane roughing pump (~50 l/s or 180 l/min). The roughing pump keeps the turbo pump forepressure in the range of 10^{-4} torr. The pressure is measured by a Varian 0564-K2500-303 Bayard-Alpert style ionization gauge with a Varian Multigauge controller (Part

No. L8350301). All vacuum seals use fresh copper gaskets to maintain a high quality vacuum.

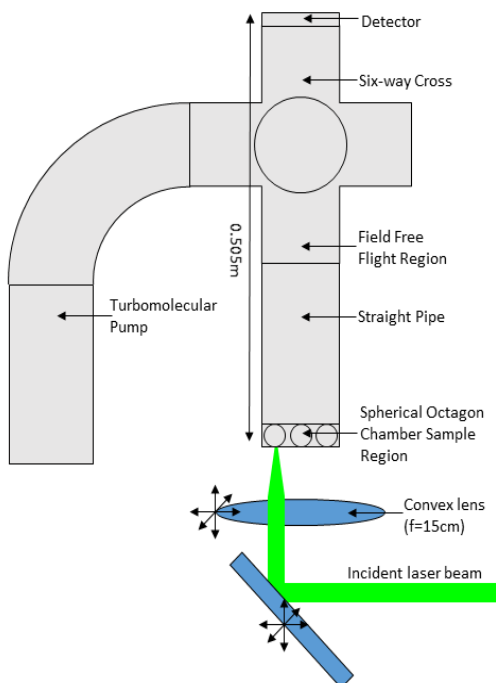


Figure 3.1 The Vacuum chamber overview. The turbomolecular pump is mounted off to the side of the six-way cross. The detector is mounted at the top of the six-way cross. The incident laser beam enters chamber from below via a 6" CF window port at the base of the Spherical Octagon Chamber. A straight pipe serves as an extension of the flight tube. The focusing lens and mirror are mounted on independent 3-D translation stages outside the vacuum chamber.

3.2 Detector and Data acquisition system

At top of the vertically oriented vacuum chamber is a pair of microchannel plate (MCP) detectors in Chevron mode coupled to a stainless steel sheet collector plate (see Figure 3.2). This system provides excellent gain of $\sim 10^6$ and great temporal resolution. The 0.6 mm thick microchannel plates are made of glass and have 10 μm diameter channels passing through at a 12° angle with respect to the plate surface. The channels have a 12.5 μm separation from center to center.

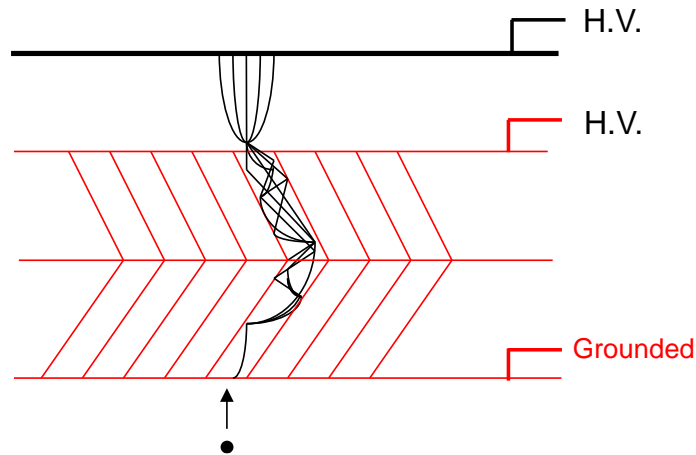


Figure 3.2 The microchannel plate detector in Chevron mode uses a stainless steel collector plate. The plates have a diameter of 25 mm, while the channels are at a 12° bias angle with a 10 μm diameter and a center to center channel separation of 12.5 μm .

Energetic charged particles striking the interior of a channel wall generate secondary electrons. This process repeats along the length of the channel to achieve the large net gain. The bias voltage accelerates the secondary electrons down the channel through the plates where the cascade process yields more secondary electrons. With the front of the first plate grounded and the back of the second plate biased at +1600V, +1700V or +1800V to record the signal with reasonable size from collection software, the two plates produce a combined gain as large as 10^6 . The front of the first microchannel plate is grounded to maintain zero field in the field free flight region. The chevron mode of two microchannel plates means these two plates are positioned with 180 degree rotation to make a “V” configuration. This setup limits the contribution of false event counts coming from back streaming positive ions producing another electron cascade after an energetic channel wall collision.

The secondary electrons are accelerated to the collection plate that is biased at the same voltage as the second microchannel plate. The electrical signal is collected after a coupling circuit and recorded by a DP211 Acqiris Technologies 8-bit digitizer board. A photodiode signal detects scattered laser light to provide an external trigger for the data acquisition. This photodiode signal is only used for triggering the acquisition. The absolute zero time is determined by detecting an

single electron signal from a negative ion spectrum. This electron signal, with 3 KeV energy, arrives at the detector 37 ns after the electrons have been created. A typically data run consists of 100 single shots, each stored individually. The acquisition program has a display window and a zoom window to monitor both the entire ion spectrum of one single shot and a specific ion peak, such as BMIM⁺, for live monitoring. The live monitor zoom window is very helpful when aligning the experimental setup.

3.3 Laser and Optics

The laser that produces the ionization is the second harmonic (532nm) of a Quanta-Ray DCR-2A ND: YAG laser operating at a 10Hz repetition rate. This repetition rate is much slower than necessary for the $\sim 10 \mu\text{s}$ flight time of the ions we observe. A different laser, running at rates up to 1 KHz have made data collection much faster in some systems, but attempts to detect high values of q/m would still necessitate high numbers of ions, producing the resolution degradation. A very high repetition rate, such as that of a typical Kerr-effect short pulse Ti:Sapphire laser (10-20 MHz) would not allow sufficient time for the ions to travel the free flight region. This could confuse ions from one pulse with those from other pulses. The spot

diameter after the doubling crystal is approximately 1 cm. Figure 3.3a shows the temporal profiles of one hundred laser shots, as measured by a photodiode. The pulse widths are nearly constant and the amplitudes have less than 5 percent (RMS) variation. Figure 3.3b shows a typical single shot. The Q-switched laser has a central peak with a full width at half maximum of 5ns, surrounded by two reduced energy peaks. The relative amplitude of the side peaks is the largest apparent variation from pulse to pulse. At higher temporal resolution,

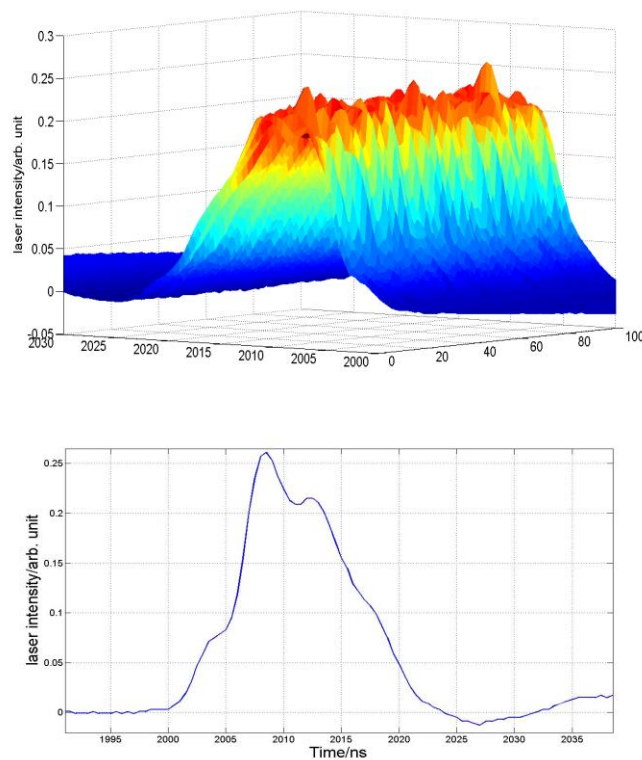


Figure 3.3 Temporal profile of ND: YAG laser pulses. In a) 100 laser shots show a relatively stable pulse with amplitude fluctuations less than 5 percent. In b) a single shot laser temporal profile shows a central peak width of less than 5ns.

we expect the output to show mode beating, as the linewidth is larger than the Fourier transform limit of the 5 ns pulse duration. The average power of a single laser pulse was typically 2 mW as measured by a thermal power meter (Newport model 835) for a net energy per pulse of 200 μ J.

Since we only needed a small fraction of the laser output we used the reflection from the front face of a prism placed in the laser path. We further reduced the laser power using a series of neutral density filters. The beam enters the vacuum chamber from below, having been reflected up through the bottom window of the chamber. Inside, it again reflects from a mirror mounted at 45° with respect to the optical table. A three dimensional translation stage, mounted outside the vacuum chamber, positions a 15 cm convex lens to focus laser beam to a 50 μ m spot on the sample surface. The translation stage allowed us to scan the position of the spot over the entire sample. The focused laser spot displayed higher order modes with complicated structure when imaged on black burn paper. Inside the vacuum chamber, the top-down illumination system reflects the beam to the target surface.

3.4 Laser ionization sample assembly and exchange

The multiphoton source region(See Fig.3.4) consists of a stack of five identical stainless steel square plates (eV parts series C, Kimball Physics Inc.) whose dimensions are

1.4"×1.4" with a 0.187" diameter round hole in the center. Alumina spacers

isolate the plates from one

another. The second plate is grounded and the bottom one is biased at +3kv to detect positive ions or -3kv to detect negative ions. The space between these two plates provides the acceleration field. The other three plates can be used as an Einzel lens to enhance the collection efficiency; however, these three plates were held at ground to simplify the ion flight path for the work reported in this thesis. A piece of 1 cm wide steel stainless shim stock, welded on the edge of

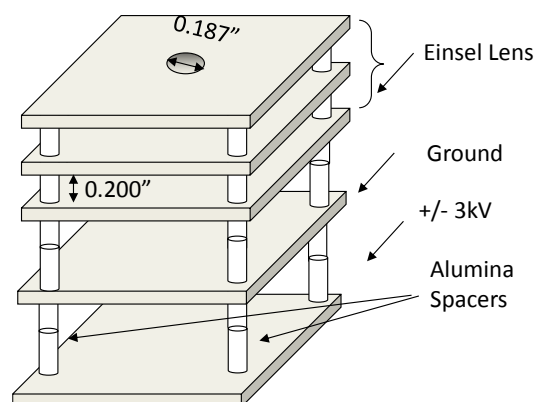


Figure 3.4 The ionization source assembly, including an Einzel lens stack. Stainless steel plates are electrically isolated from each other by alumina rods and spacers. The plates are 1.4" squares, 0.026" thick.

the plate provides the voltage lead. The 2.75" feedthrough flange with four electrode outputs is mounted on the side window of the octagon chamber. This multi-plate stack structure hangs above the bottom 6" CF window, fastened to the side wall by a Groove Grabber system (Part No: MCF600-GrvGrb-C01, Kimball Physics Inc.) which itself is mounted to the groove inside the chamber bottom.

The sample holder, a square copper plate with a 5mm diameter well, 0.4 mm deep as in Figure 3.5 sits in the center of the bottom plate, maintaining good electrical contact. The well in the sample holder is either filled with RTIL or holds a small metal piece as a test sample.

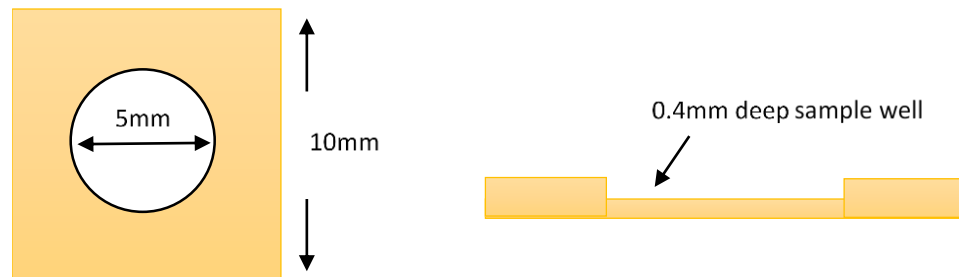


Figure 3.5 a) Top view of the sample holder. 10mm square with 5mm diameter well. b) Side view of sample holder. 0.8 mm height with 0.4 mm deep well in center.

The laser beam comes up from below through the bottom of the 6" CF window and reflects down to the sample in the holder. The top-down illumination system (Fig.3.6) consists of a mirror mounted inside the chamber to reflect the laser beam to the sample surface.

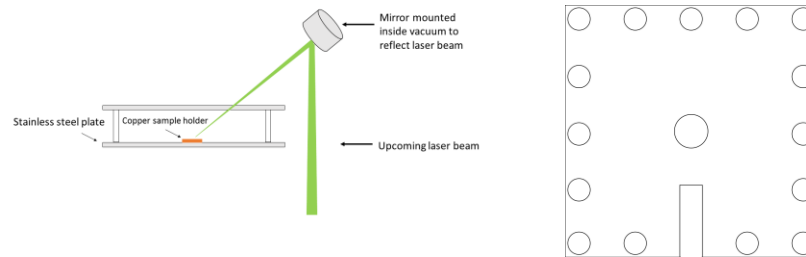


Figure 3.6 The top down illumination system (a), and a drawing (b) of the stainless steel plate with a slit.

The mirror is clamped to a steel stainless ring that is bolted to one end of a wide stainless steel plate which itself is mounted to another groove grabber attached to the bottom of the chamber. The mirror is tilted at a 20° angle from the horizontal so that the laser beam hits the target with an incident angle of 50° . There are two 1 mm wide 0.4 inch long slits cut into the sides of the 2nd and 3rd accelerator assembly plates to let the laser beam pass. The beam is focused by a convex 15 cm lens, outside the vacuum chamber, to form a spot on the target that is approximately elliptical, approximately $50\text{ }\mu\text{m}$ wide and $80\text{ }\mu\text{m}$ long. We

measured the spot size by burning a piece of metal sheet outside of chamber in the atmosphere and measuring it with an optical microscope.

In order to change samples, it is necessary to vent the chamber to atmosphere and open it. Originally, we had used the bottom window as a point of entry; however, that required realigning the accelerator stack and the focusing lens after each opening. So, we instead developed an improved system where we removed one of the side flanges on the spherical octagon chamber. This method required removing the sample holder from the side window by carefully using tweezers, but it had no effect on the top-down illumination system, the external optics, nor on the electrical connections to the chamber. This method allowed us to change samples in a few hours, with most of that time being the time required to pump the system back to a high vacuum.

3.5 System Calibration

When the system gain is set to see small signals, the larger signals can easily exceed the range limit of the collection software. We degraded the system gain either by decreasing the detector voltage or by inserting a 10 dB attenuator to gather high intensity ion signals. To determine the scale factor so that we could connect the two types of experiments (with and without the 10 dB attenuator, for example), we followed this procedure. To calibrate the signal with the 10 dB attenuator, we recorded a series of 100 laser shots while monitoring the BMIM⁺ ions. We repeated this process for runs with and without the 10 dB attenuator at three different laser powers of 0.6 mW, 1 mW, and 2 mW. Figure 3.7a shows 100 shots of data summed under 1 mW laser intensity. The large peaks in figure 3.7a were taken without the attenuator; whereas the smaller peaks used the 10 dB attenuator. The ratio between the average peak amplitudes of runs under changed conditions represents the gain scale factor. Figure 3.7b plots integral signal size under different laser intensities. The error bar is the standard deviation of multiple measurements under same conditions. The 10 dB attenuator reduces the signal size by factor of 9.87, ($\pm 3\%$) which is the slope of the linear curve.

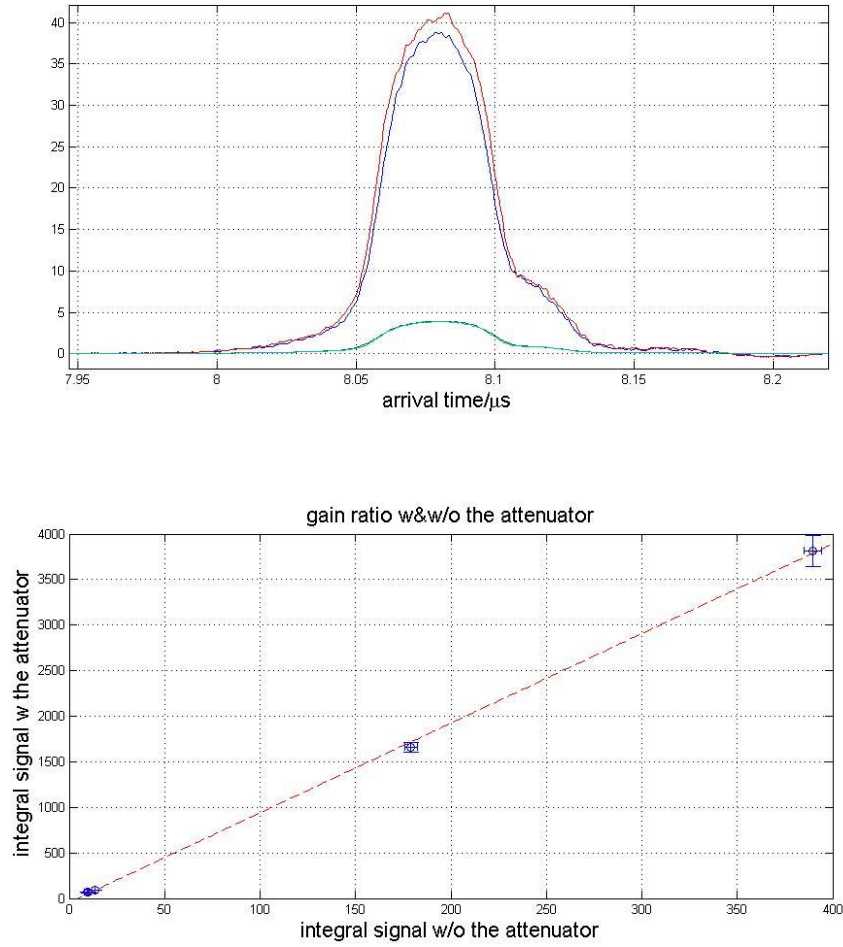


Figure 3.7 Calibrating the attenuator. In (a), data from 100 laser shots is summed to show two examples near the BMIM^+ ion arrival time with and without the attenuator near 1 mW laser power. In (b) a scatter plot of the integrated BMIM^+ signal with and without the attenuator at laser powers of 0.6mW, 1mW and 2mW. The slope is 9.87 with a 3% uncertainty.

We repeated this process to compare the gain with 1.7 kV and 1.8 kV bias on the multichannel plates, as shown in Figure 3.8. Figure 3.8a shows the integrated signal of 100 shots under 1 mW laser intensity. Figure 3.8b curve shows the comparison of the integrated signals at the three laser powers at the two different microchannel plate biases.

The slope shows a gain ratio of 2.47 ($\pm 10\%$). The purpose to have two different voltage gains is to adjust the output signal intensity to make sure the measurement is not out of range for the data acquisition process.

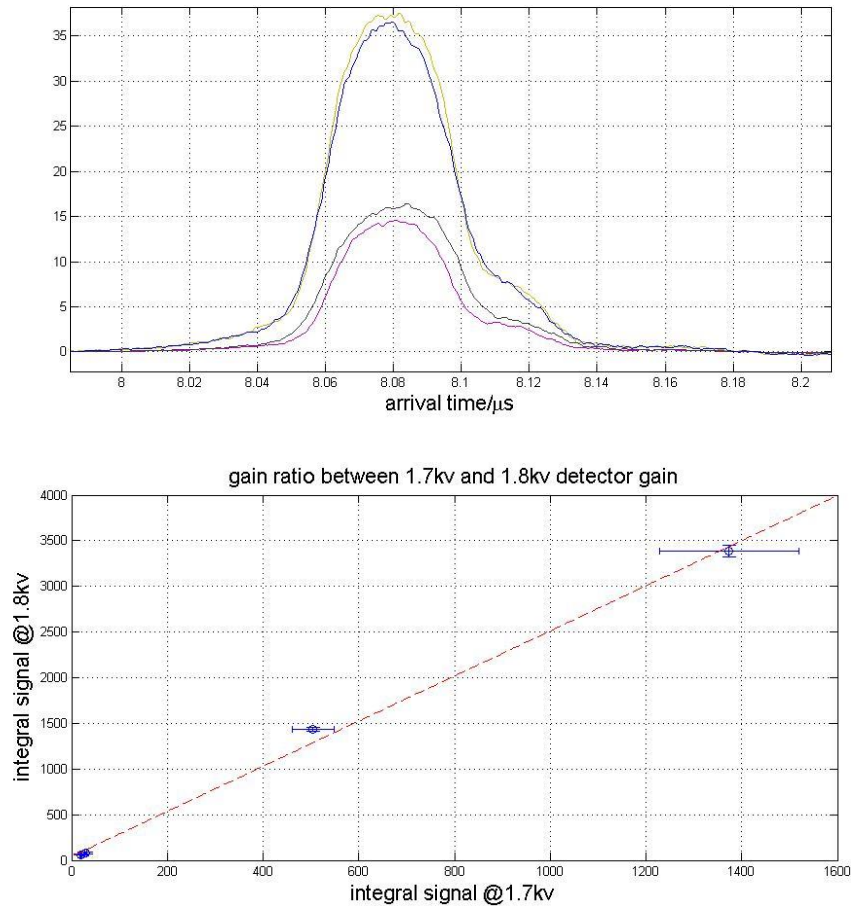


Figure 3.8 Calibrating the multichannel plate gain. In (a), data from 100 laser shots is summed to show two examples near the BMIM^+ ion arrival time with the channel plate voltage set to 1.7 kV and 1.8 kV. In (b) a scatter plot of the integrated BMIM^+ signal at three voltages. The slope is 2.47, with 10% uncertainty.

Chapter 4

Non-linear Production Process and Limits on Resolution

This chapter displays the mass spectrum generated in our apparatus and discusses the resolution decreases with increasing signal size.

Protein and peptide identification in proteomics work strongly relies on the ability to distinguish ion species and isotopic structures from a vast cluster of ion species. Conventional MALDI, using high acceleration voltages and delayed extraction is proficient in determining heavy mass ions. In the work presented in this thesis, we have used a low accelerating voltage and no delayed extraction to study why the resolution decreases with increasing signal sizes.

4.1 RTIL data

As introduced in sec. 3.4, the sample holder is either filled with RTIL or holds a small piece of metal. Figure 4.1 displays a typical average mass spectra of 100 laser shots on RTIL with +3 kV acceleration voltage and 2.5 MW/cm^2 laser intensity. The dominant peaks are BMIM⁺ with an approximate mass resolution of 150 and imidazolium⁺ which is the main fragment from unimolecular decay of BMIM⁺. There are ion peaks at atomic mass numbers 207 and 118 which are Pb⁺ and Sn⁺, the constituents of the solder that binds two copper pieces to make the sample holder. The minority peaks are atomic mass number 23 and 39, i.e. Na⁺ and C₃H₃⁺, which are contaminants on the sample

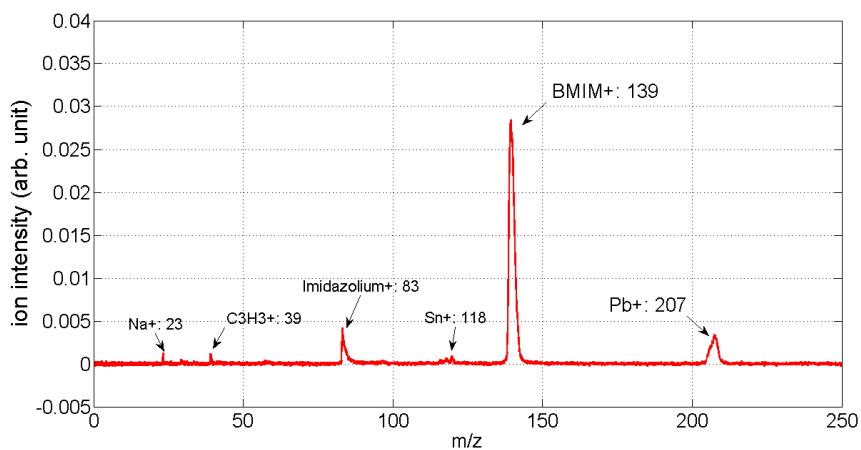


Figure 4.1 Average mass spectra of 100 laser shots on RTIL with 3 kV acceleration voltage and 2.5 MW/cm^2 laser intensity. BMIM⁺ and imidazolium⁺ are ionized from RTIL. Pb⁺ and Sn⁺ are components from solder paste on sample holder while there are minor contaminants at atomic mass number 23 and 39.

surface that occur during the sample preparation.

4.2 Nonlinear ion production process

The ion desorption process exhibits a strong power dependence at power densities below 10 MW/cm^2 . Figure 4.2 shows the average BMIM⁺ ion signal (over 100 laser shots) as function of laser intensity. The average BMIM⁺ production shows a strong nonlinear growth below 10 MW/cm^2 and rises more slowly above that.

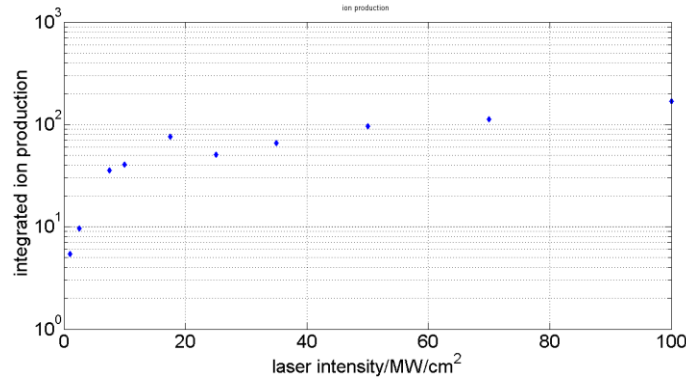


Figure 4.2 BMIM⁺ average 100 shots integrated signal as function of laser intensity in logarithmic scale. Ion production experiences rapid rise below 10 MW/cm^2 and slower growth above. Data are taken under 3kV acceleration voltage and 50cm free flight distance.

Figure 4.3 plots BMIM⁺ peaks in the averaged 100 laser shots data with low and high laser intensity, i.e. 2.5 MW/cm^2 and 50 MW/cm^2 , from the increasing region and plateau region in Fig. 4.2. The resolution is worse as average ion production signal goes stronger with high laser power intensity.

Such a rapid nonlinear increase in the signal size, and such a change in the line shape, suggests that the shot to shot variation of the spectra

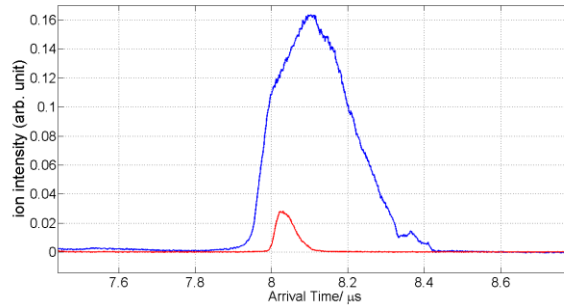


Figure 4.3 average BMIM⁺ peak of 100 data shot run at different laser intensities. Red is 2.5MW/cm². Blue is 50MW/cm².

might be very large. To illustrate the shot to shot variation, Figs. 4.4 and 4.5 show heatmaps of a single set of 100 laser shots under relatively low (4.4) or high (4.5) laser intensities near the arrival time of the BMIM⁺ ion. The color bar represents the raw ion signal intensity in volts. Although the higher intensity produces more ions and broader peaks than the low intensity spectra as shown in Fig. 4.3, the most remarkable feature is the wild arrival time variation from shot to shot.

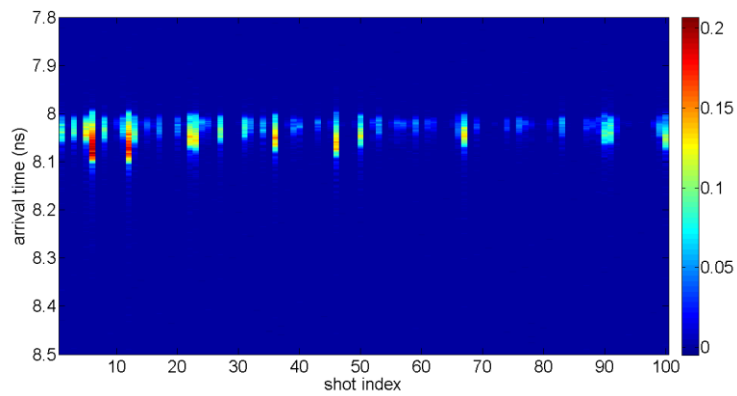


Figure 4.4 Heatmap displays BMIM⁺ peaks over the course of 100 data shots run at 2.5MW/cm² laser intensity. Color bar represents raw ion signal intensity in volts.

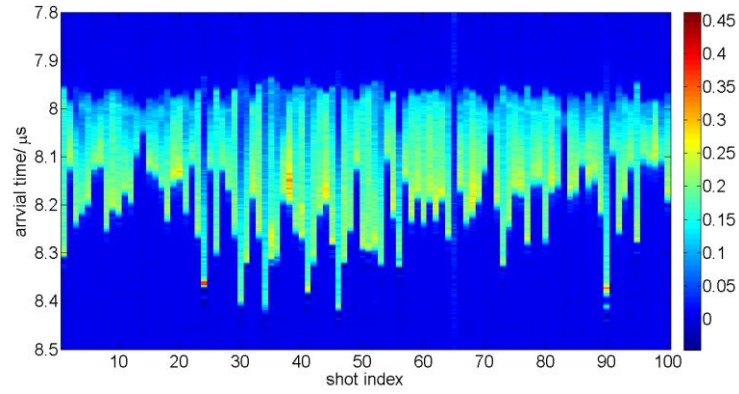


Figure 4.5 Heatmap displays BMIM⁺ peaks over the course of 100 data shot run at 50MW/cm² laser intensity. Color bar represents raw ion signal intensity in volts.

Figure 4.6 shows the variation from shot index number 71 to 74 from Fig. 4.5. Since all the experimental parameters were fixed, and the

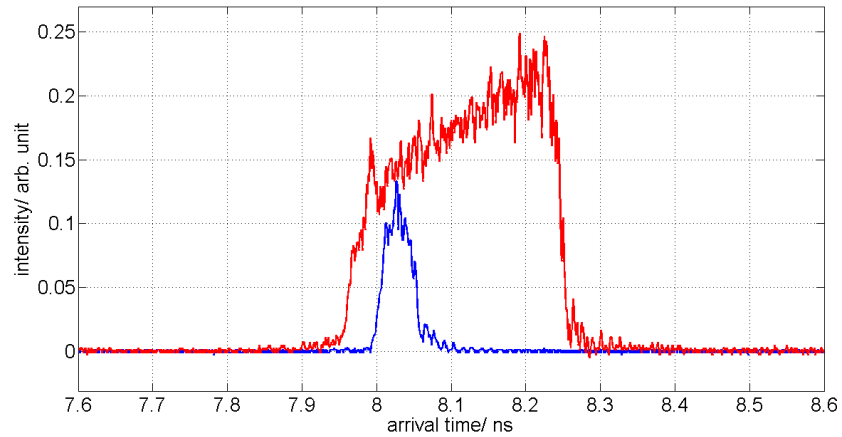


Figure 4.6 BMIM⁺ peaks in shots whose index numbers are 71(weaker signal) and 74 (stronger signal) from high laser intensity data as in figure 4.5

laser intensity fluctuations were less than 5%, we believe the large variation in signal size is due to the strong non-linearity coupled to the varying hot spots made by the temporal and spatial variation of the laser. Typically we see about 1 cm^{-1} linewidth, where the Fourier transform limited pulsed pulse would be 1000 times narrower. So, a limited pulse has a lot of temporal mode beating that gives “hot” spots lasting for tens of picoseconds, well below what we can see with our photodiode. We can see the temporal shot to shot variation in that the side peaks in the time profile tend to vary much more than the overall energy. Sometimes the early side peak is smaller than late one, sometimes reversed. The spatial modes are even worse. The laser spot is pretty far from a single mode Gaussian beam – even before the doubling crystal, which emphasizes hot spots. We routinely see structure in our burn patterns such as hot areas that are a millimeter or out of 1 cm beam. So, this likely gives rise to (non-repeatable) hot spots that are ten times smaller than nominal focused laser spot. All of this means that the small time and small space variation of the laser pulse intensity is much greater than 5% overall energy variation we observed.

4.3 Resolution Degradation

4.3.1 Ion production dependence

Figure 4.3 shows that the resolution has degraded in the shots with higher laser intensity. Figure 4.6 shows that, even with the same nominal laser intensity, a spectrum with high ion production has significantly worse resolution than a spectra with lower ion production.

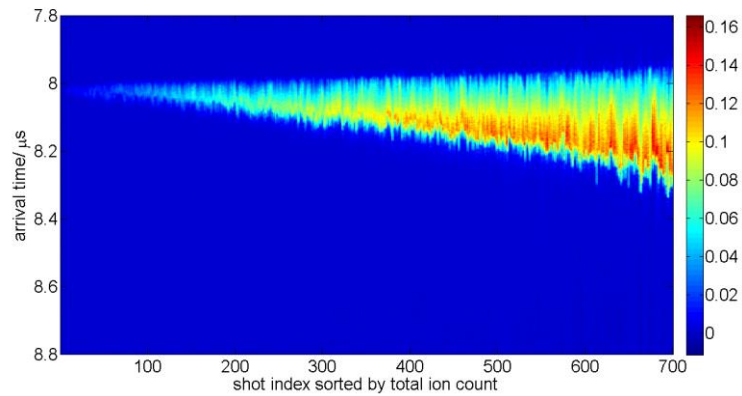


Figure 4.7 Heatmap displaying a 700 shot data run of positive 3 kV BMIM⁺ peaks. Shot index are sorted by total ion production. Laser intensity is 50 MW/cm². Free flight distance is 50 cm.

To explore the pattern of resolution related to ion production, Fig. 4.7 represents 700 laser shots with the nominal laser intensity fixed at 50 MW/cm², showing the data near the positive BMIM⁺ ion time location, following 3 kV acceleration and 50 cm of free flight distance. Data are from different dates and different sample locations by moving laser spot locations are combined in this figure. The heat map in Fig. 4.7

differs from that in Figs. 4.4 and 4.5 by being sorted in order of increasing total ion signal.

This shows that the peak width grows rapidly with increasing signal size, decreasing the resolution. Moreover, the peak shape distorts and becomes very asymmetric. Figure 4.8 shows the time signals for index numbers 70 and 630 of Fig. 4.7 to illustrate both of these effects. Note also, that Fig. 4.8 shows a sharp cut-off on the late arrival side.

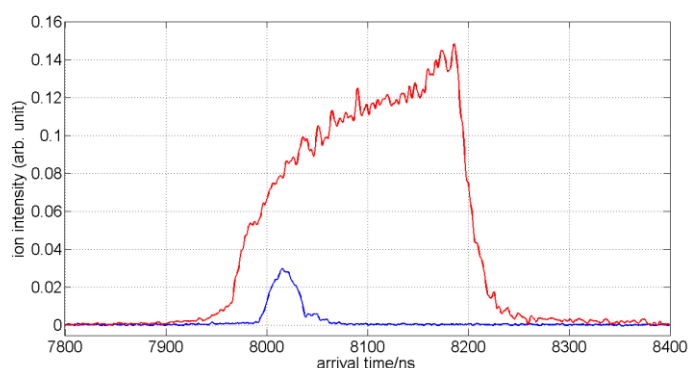


Figure 4.8 single traces of high (index 630) and low (index 70) BMIM⁺ peaks. High ion intensity peak shape becomes asymmetric and slow side has sharp cut off edge.

As the total ion signal grows, the BMIM⁺ peak broadens and distorts. Because it distorts so much, it is no longer sufficient to simply classify it according to a FWHM. So, Fig. 4.9 shows Fig. 4.7 with green crosses marking the earliest and latest arrival times of the BMIM⁺ ions.

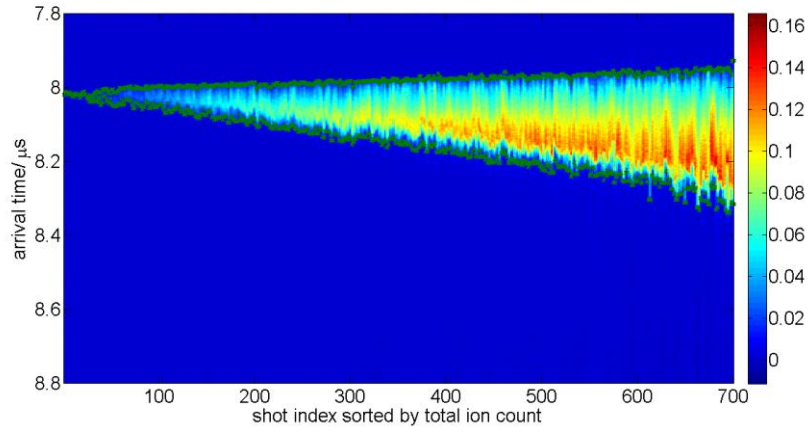


Figure 4.9 Heatmap as figure 4.7. Green cross dots are earliest and slowest ion

Figure 4.10 illustrates the process to find out these arrival times with single shots in Fig. 4.6. Within a time window larger than the broadest

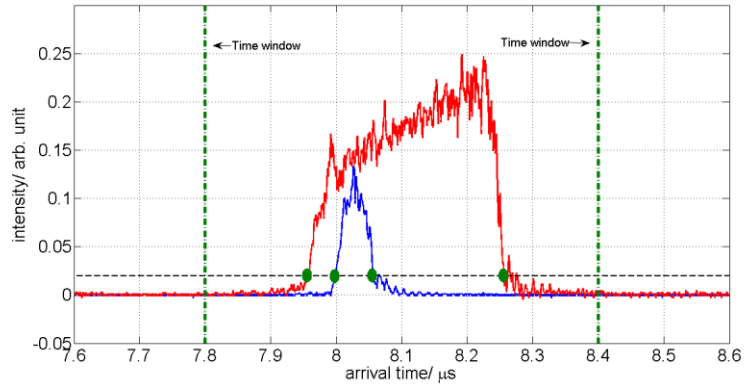


Figure 4.10 process to find out earliest and latest BMIM⁺ ion in each single shot

BMIM⁺ peak, we have determined the times when the signal is 10% of its maximum value during the peak. We will define a full time width of

each peak as the difference between the earliest and the latest of these points. Figure 4.11 represents the growth of the BMIM+ full width versus total summed ion signal intensity.

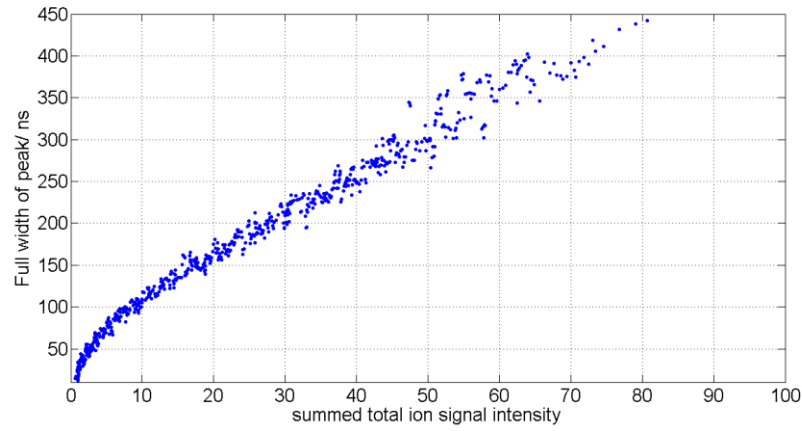


Figure 4.11 BMIM⁺ peaks full width in terms of total ion intensity. In high intensity region, it is a linear curve. Data are positive 3 kV and 50 cm free flight distance.

4.3.2 Ejection time spread in resolution

The two major contributions to a changing width are changes in the initial velocity distribution and changes in the initial ion ejection time.

Chapter 2 showed the relationship between energy (or velocity) spread and arrival time spread to be

$$\frac{dv}{v} = - \frac{dt}{t} = \frac{dE}{2E} \quad 4.1$$

Under same acceleration voltages, if the resolution degradation is mainly due to initial velocity spread, the time spread should be linearly dependent on the travel time or the free field flight distance. In our experiment, we placed the detector at three different locations, specifically 50 cm (called “far”), 25 cm (called “intermediate”) and 10 cm (called “near”) from the ion desorption source. Figure 4.12 shows the full widths of the BMIM⁺ peaks collected with the three detector positions. The blue dots are results from the 50 cm free flight (far detector). The red dots are results from the 25 cm free flight (intermediate detector), and the green circles are results from the 10

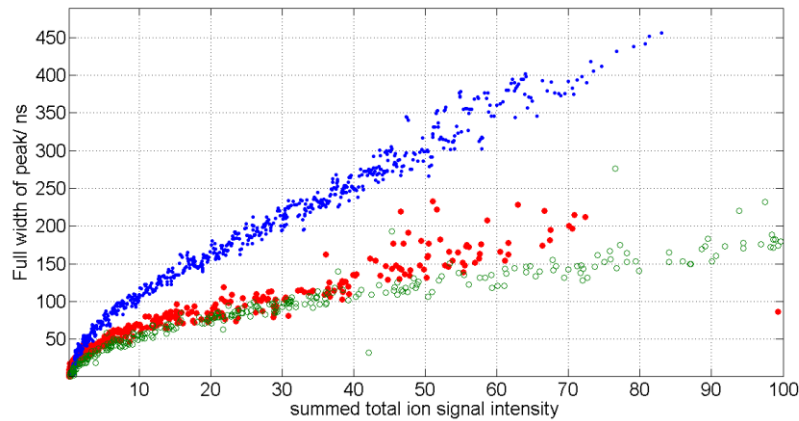


Figure 4.12 BMIM⁺ peak width versus total ion signal from 50 cm (blue), 25 cm (red) and 10 cm (green) detector position. Data are taken with 3 kV acceleration voltage and 1.7 kV detector gain.

cm free flight (near detector). The peak widths follow the same shape of functional dependence for the near and intermediate detector positions. This suggests strongly that the width increase is not due to a velocity spread. If the width were due to a velocity spread, the red

circles would have risen at a rate 2.5 times faster than the green circles. The far detector data seems inconsistent with this at first sight; however, most of that data shows a lower total signal size. Our simulation in the next chapter will show that this apparent increase is due to the expansion of the ions to fill a spot much larger than the detector, effectively reducing the detector efficiency by a factor of 2 approximately. If the data were corrected for this loss of ions, all three detector position would produce the same curve, demonstrating that velocity spread is not the major cause of the linewidth change.

Before check width dependence on energy, we need to know the detection efficiency of the microchannel plate detector is dependent on the incident impact energy of an incident ion. In this experiment, 2kV and 3 kV are our standard acceleration voltages leading to different detection gains. To calibrate the efficiency with different energies, we collected BMIM⁺ data with 2 kV and 3 kV sequentially under the same detection voltage and laser intensity conditions. Sorting the signal size with different total energies, the correlation between collected ion productions explicitly illustrates the efficiency difference BMIM⁺ ions with either 3 kV or 2 kV total energy (Fig 4.13). Assuming that the total distribution of the production of BMIM⁺ ions was the same for the

sequential runs, we find that the higher energy ions produce a signal at the detector that is $1.95 (\pm 3\%)$ times larger than the lower energy ions.

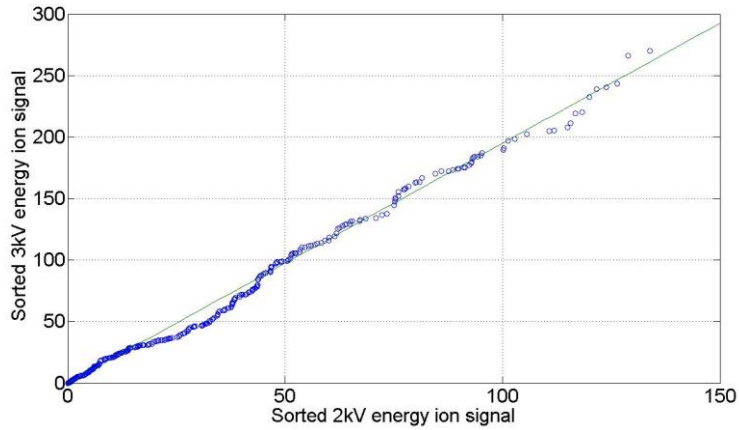


Figure 4.13 Correlation of BMIM⁺ data taken with 3kV and 2kV acceleration voltage. The detection gain ratio is 1.95 to calibrate ion data with different energy.

As an additional check on the origin of the linewidth growth, we measured the dependence of the linewidth on the acceleration energy.

Figure 4.14 shows the growth of the peak width of the BMIM⁺ when accelerated by either 2 kV or 3 KV. If the linewidth were due to a velocity (or energy) spread, then the increasing the acceleration energy would reduce the linewidth for two reasons: (1) the initial energy spread would be a smaller fraction of the total energy, and (2) the arrival time would decrease. The 2 kV summed ion signal intensity has been increased by the 1.95 factor in accordance with the reduced detection efficiency shown in calibration.

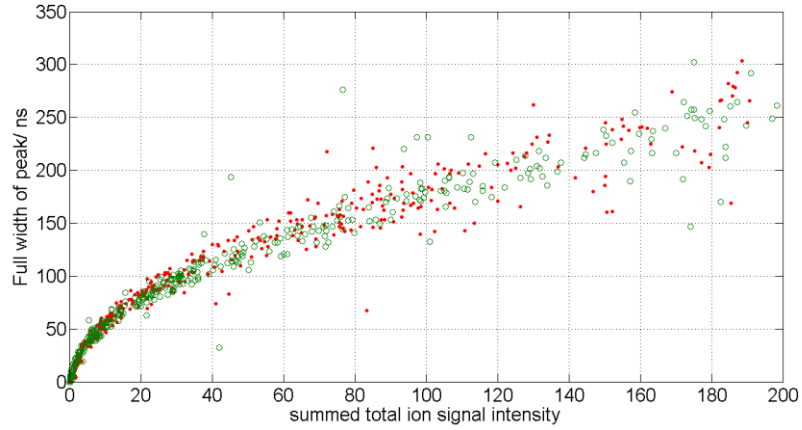


Figure 4.14 Scattered dots display of the BMIM^+ peak width in term of total ion production. Green dots represents 3 kV total energy data while red dots represents 2 kV energy data. Both data are taken in the near detector setup, i.e. 10 cm free flight distance.

Figure 4.15 represents the peak width growth with ion signal increase for different initial electric field amplitudes. All of these BMIM^+ data

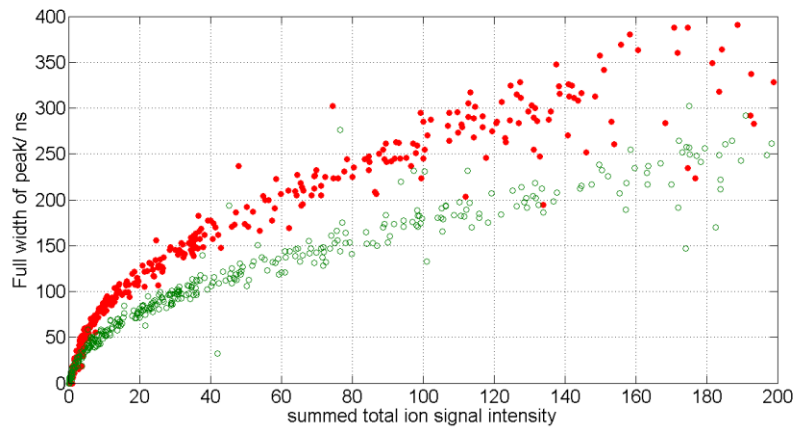


Figure 4.15 Scattered dots display BMIM^+ peak width in term of total ion production. Green dots represents 3 kV energy in 0.4 inch long electric field. Red dots represents 1 kV in first 0.4 inch electric field and 2 kV in next 0.4 inch electric field with 3 kV total energy.

were taken with the detector in the near position (10 cm free flight).

The green dots are data taken in the normal condition of 3 kV accelerating voltage across with a 0.4 inch plate separation. To change the field without changing the total energy, we applied 1 kV across the first set of plates (0.4 inch separation), followed by 2 kV across the second set of plates. For these data, the red dots in Fig. 4.15, the extraction field is smaller by a factor of 3. This shows that under same ion production conditions, the peak width grows faster in a weaker extraction field.

To verify if the peak broadening is universal, rather than being a characteristic of the RTIL (which does undergo a unimolecular decomposition during the free flight), we used a polished piece of metal containing both chromium and iron. Figure 4.16 displays 400 laser shots sorted by the total ion count (with 3 kV acceleration volts and a 50mW/cm^2 laser intensity). Figure 4.16 shows a similar peak width increase with ion signal growth.

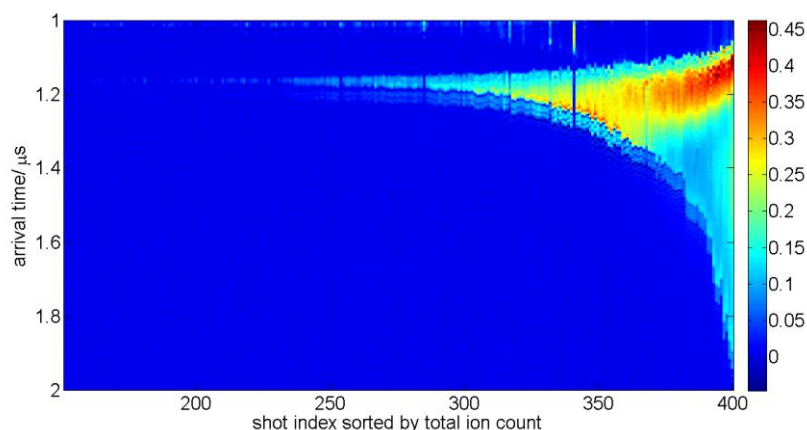


Figure 4.16 Heatmap displaying 400 shot data run of chromium and iron metal which sorted by total ion count. Data taken with positive 3 kV and 50 MW/cm² laser intensity in near detector setup.

Figure 4.17 represents the full peak width of Cr⁺ (red dots) and BMIM⁺ (green circles) related to total ion signal size. The full peak width

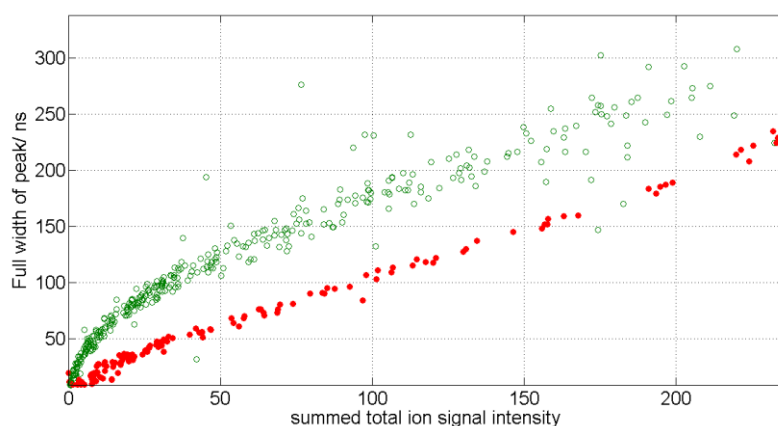


Figure 4.17 peak width versus total ion signal intensity. Red dots are Cr⁺. Green circles are BMIM⁺. Both data are taken with positive 3 kV in near detector setup.

broadening effect is universal instead of unique character of BMIM⁺.

This chapter has shown that the mass arrival times broaden with increasing total ion production causing a degraded resolution when all other experimental conditions (acceleration voltage and field, travel distance, and laser power) are held constant. For ions with same charge to mass ratio, the resolution as measured by arrival time depends on initial electric field strength rather than on the total energy gained from the acceleration field. Thus, the resolution degradation is not due to an increase in the initial ion thermal distribution. Instead the initial ejection time spread has the greatest contribution to the peak width broadening. One hypothesis is that space charge from the ejected ions will weaken the electric field near the ion source to prevent other ions leaving until the already ejected ions are accelerated out of the source region. This leads to an initial ejection time spread that degrades the resolution. We will elaborate models that simulate this space charge effect fully in the next chapter.

Chapter 5

Simulation

As shown in the last chapter, ions continue to escape into the acceleration region for a longer time as total ion production grows. In this chapter, we first present a simple model to simulation space charge effect. Then mean field model simulates space charge effect and image charge effect at large scale of ion quantities. Ion reservoir modification describing initial ion distribution successfully fits experiment data, combining with mean field model. Lastly, slices model with GPU computing technique dispels concern of accuracy for high multiplier in mean field model.

5.1 Particle Solutions of the Space

Charge Model

To study the behavior of a large quantity of collisionless ions, we started by simulating each individual ion's trajectory, solving the motion and the electric fields of all the ions simultaneously. Equation 5.1 shows the force on each individual collisionless ion, where the first term is the force from the other ions and the second term is the force from the external applied electric field. Equation 5.2 shows the differential ion movement under the net force.

$$\vec{F}_i = \frac{1}{4\pi\epsilon} \sum_{i \neq j}^n \frac{e_i e_j}{d_{ij}^2} + e_i \vec{E}_0 = m \vec{a}_i \quad 5.1$$

$$\vec{v}_i = \vec{v}_{i-1} + \vec{a}_i t \quad d\vec{l} = \frac{1}{2} * (\vec{v}_{i-1} + \vec{v}_i) dt \quad 5.2$$

A solution requires initial conditions for each ion. Setting those initial conditions defines a model.

For our first model we wanted to explore the effects of the ion space charge during the ions nominally free-flight to the detector. So, we assumed that the external electric field swept away all of the electrons immediately. When we used a negative 3kV bias to accelerate negative ions in the experiment, we found that the electrons arrived at

the detector in 7ns, so reversing the field will remove the electrons in a time much shorter than the ion travel time, justifying our assumption that they have been swept away. For our ion initial conditions, we used a uniform distribution over a thin disk. We chose the thickness to match the distance a free ion would travel in the applied electric field during a laser pulse time, *i.e.* 5ns. We chose the radius of the disk to match the semi-minor axis of the laser spot. This model simplifies the complex lase desorption process by only considering ions without electrons after laser pulse.

5.1.1 Matlab ode45 solver

We first used the Matlab ode45 function to solve these differential equations. Figure 5.1 shows the arrival time distribution of 100 ions

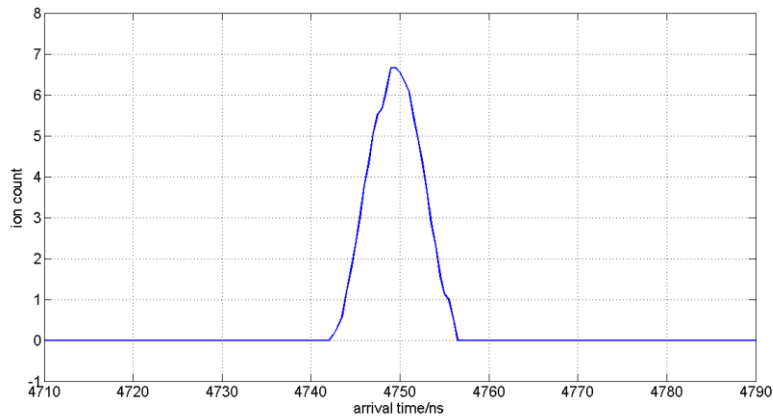


Figure 5.1 arrival time distribution of 100 ions from space charge model with Matlab ode45 solver.

whose mass is 52 atomic mass units (Cr^+) at a detector that is 50 cm from the acceleration region. When the number of ions is small (~ 100), the arrival time matches the 4749ns expectation time and the peak is symmetric.

Figure 5.2 shows similar results for 1000 ions and 8000 ions. The arrival time distribution becomes broader and starts to show asymmetry as the ion production increases. But as opposed to our experiment data, in the simulation more ions shift to earlier times than to slower times.

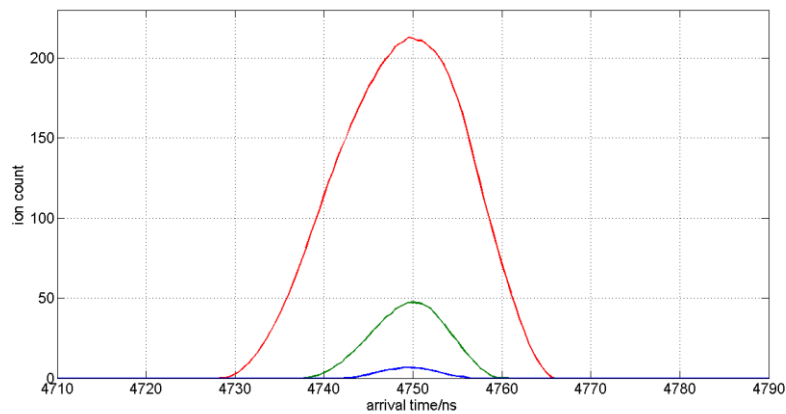


Figure 5.2 Simulated time distributions for several values of ion counts. Blue: 100 ions. Green: 1000 ions. Red: 8000 ions. Peak width is broader but there are more earlier ions instead of more slower ions shown in our experiment data.

There are a couple of crucial disadvantages with this method and model. First, the calculation is time consuming. For the 1000 ion case,

the code ran for approximately 4 hours with Intel® Core™ i7-3770 CPU and 12 gigabytes memory. For the 8000 ion case, it ran over 100 hours. Second, due to high dimensional matrix manipulation ($\sim N^2$), this method would require 12 gigabytes of memory for 10,000 hours, and would stop with an out of memory message for a calculation using over 16000 ions. This method seems unlikely to be extendable to the 100,000-1,000,000 ion cases we believe are necessary to model our experiment. In addition, the simple ion distribution in this model is unlikely to represent the real situation when a large space charge begins to affect the ions during their first stages of acceleration. In the next coming sections, other simulation models and techniques will eliminate these issues and explain our observed ion behavior.

5.1.2 Customized Fixed Time Step Solver

Initially, the ions move very slowly, and we did not expect that the solution should require sophisticated integration techniques. So, we wrote our own matlab code to solve for the ions motion using a fixed calculation time step of 0.5 ns. The general process is similar to using the ode45 function to solve the differential equations of Eqs. 5.1 & 5.2. However, by avoiding the adaptive time steps of the Matlab ode45 function, we have significantly reduced the calculation time. Figure 5.3 shows that the Matlab solution and our code produce very similar

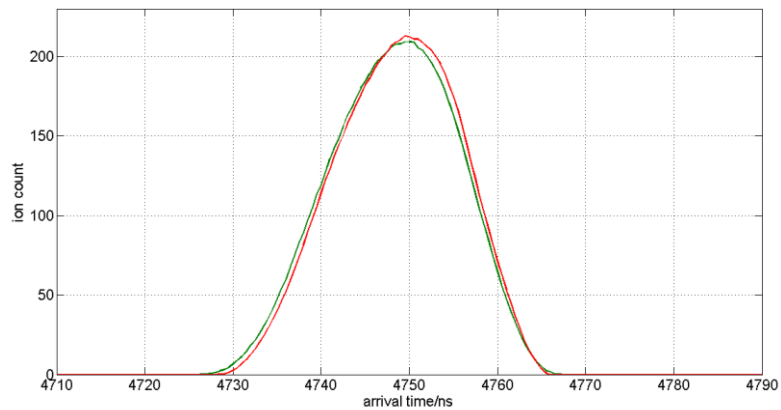


Figure 5.3 8000 ions simulation compare ode45 runtime with own fixed time step solver. The final distributions are almost the same and calculation time is much shorter with fixed time step solver.

results for the 8000 ion arrival time distribution. The calculation time with this fixed time step code is approximately 24 hours, which is less than one fourth of calculation time using the ode45 solver.

5.2 Mean Field Model

As stated above, the ion-ion iterative binary interaction approach to delaying space charge has severe limits on the total number of ions we can start in a simulation. Moreover, the ion arrival time distribution shows calculated this way does not show the enhanced delay as we observed in experiment. In this section, we will introduce several improvements to the basic model: we will include the effect of an image charge created by the first acceleration plate being held at a constant potential, and we will extend the calculation to larger total charge by introducing a multiplier, so that each point represents a large number of ions within a small volume.

5.2.1 Image Charge Effect

The acceleration plate and the sample holder are both conductive and held at a constant potential. Consequently, any net positive charge above the plate will create a negative image charge on the backside of the plate to cancel out the transverse field, leaving the net field perpendicular to the plate. This image charge will slow the leaving ions and should therefore reduce the final arrival time for large ion populations. Figure 5.4 shows a simulation of the time distribution at 50cm detector setup for 1000 ions, again starting in a uniform disk with zero initial velocity, calculated with our own fixed time step code. As

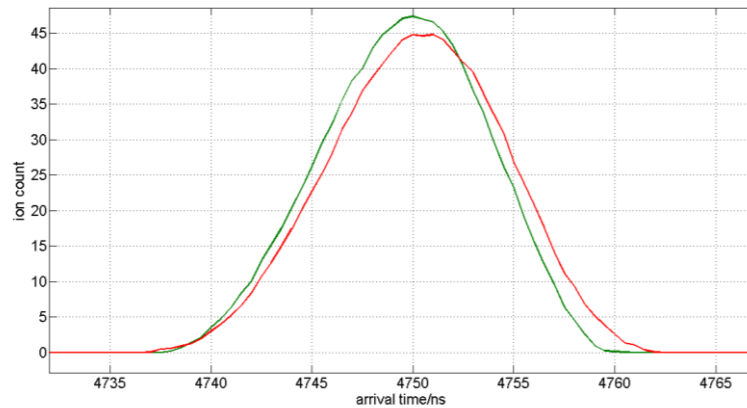


Figure 5.4 1000 ions simulation comparison without (green) and with (red) an image charge, calculated using the fixed time step code.

expected, the image charge results in a slight delay of the arrival time distribution. However, to extend this approach to large numbers of

ions, we had to use a cell approach, where each cell represented a large number of ions.

5.2.2 Mean Field Model with Multiplier

The limits on our by computer hardware made it impossible to simulate tens of thousands of ion trajectories. In our mean field model, each single ion cell represents a large number (called a multiplier) of ions in the same cell. The trajectory of a cell is calculated just if a single ion were at its center location, but this trajectory is then applied to all the ions in that cell. The electric force on each ion in the cell is calculated from the fields due to all other cells, the image charges and the applied electric field. This model is similar to the widely used particle in cell (PIC) model of ion simulation [37, 38, 39]. Our model differs from PIC models by not allowing ion exchange among cells and by our assumption that ions in the same cell produce no average force on the cell center location. By varying the multiplier (the net number of ions in a cell), we could easily extend our code to an arbitrarily large total number of ions.

In figure 5.5, we compare a simulation of 40,000 versus 2,000,000 BMIM⁺ ions, using 2000 cells with multipliers of 20 and 100, respectively. Ions are initially uniformly distributed in a 1 μm high disk

with a 25 μm radius. This simulation uses a near detector (at 10 cm), and shows a large shift towards longer times, similar to our experiment.

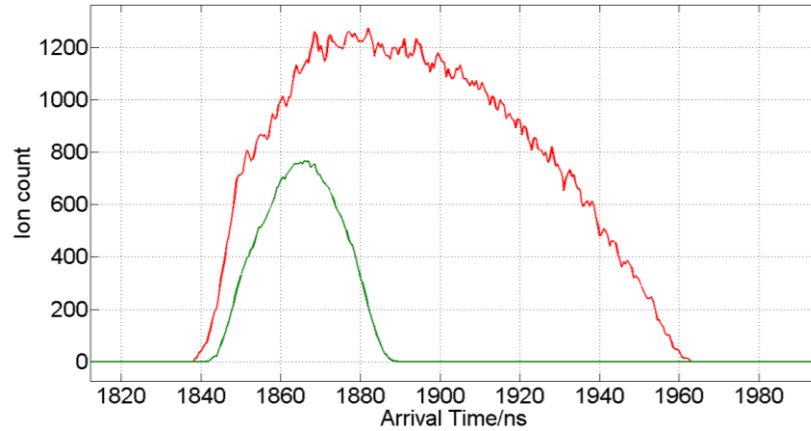


Figure 5.5 Time distributions of 40 thousands (green) and 0.2 million (red) ions generated using the mean field simulation code.

For a sufficiently large number of ions, the combined fields of the ions already moving out into the acceleration region, and the image charge of those ions behind the acceleration plate surface, can entirely cancel out the applied acceleration field, and even reverse its direction. In this case, some ions can be accelerated back towards the acceleration plate. Thus the net number of ions leaving the acceleration plate can oscillate, as shown in Fig. 5.6. For this figure, we used a total of 0.2 million ions distributed uniformly in a 1 μm high disk with a 25 μm radius. We do not expect this oscillatory behavior to be observed at this level because it depends on the removal of all the electrons so that

only ions remain. If the ion density is sufficiently high to cancel the acceleration field, then not all electrons will be swept out, and their movement will then damp out the oscillations. However, in figure 5.6, the average loss rate extends to times as long as 100 ns, ten times longer than the laser pulse time, and this, we believe, is the origin of the shift of the arrival peaks toward longer times.

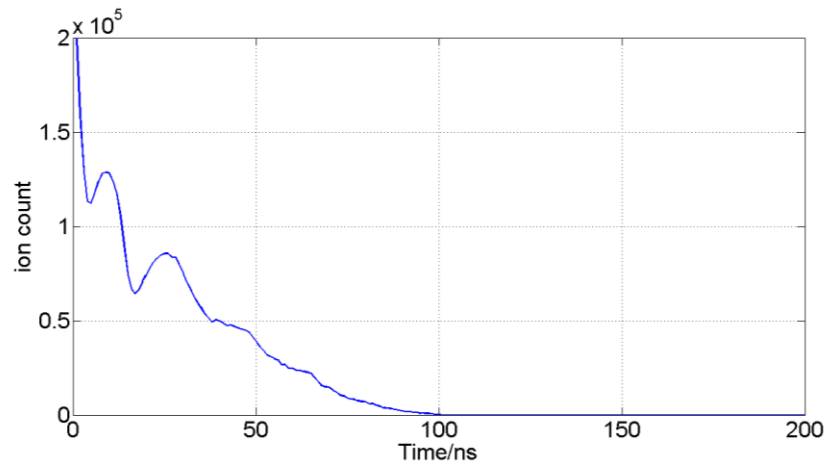


Figure 5.6 Total ion counts near acceleration plate from 0.2 million ions simulation with mean field simulation model. Ions oscillate near surface indicates ion interaction field exceeds external electric field.

5.2.3 Ion Reservoir Model

It is beyond the scope of this work to include the electron behavior under conditions where the space charge and the image charge both cancel the acceleration field. Instead, we have used an ion reservoir model, for which we have manually constructed a thin region on top of the acceleration plate filled with an electrically neutral combination of ions plus electrons, in which the net electric field is zero. Ions initially escape from the reservoir at the common laser desorption initial velocity of 1 km/s. However, once the longitudinal net electric field at the location of the ion in the reservoir is reduced below a launching threshold field, which is a small fraction of the unshielded acceleration field, the ion ejection ceases. As the ejected ions continue to move away, the field will again decrease, allowing more ions to escape (with their equivalent electrons flowing into the acceleration plate). The net effect is that the ion production rate matches the rate that ions leave the acceleration region. This model reduces the ion oscillations and produce a slowly decaying ion source after the laser pulse. Figure 5.7 shows the results of this model compared to experimental work with the detector at 10 cm from the source. The green circles are time distributions of BMIM+ sample with 10 cm detector setup at 3 kV acceleration volts. The red curve with dots are simulation results using

a reservoir thickness of $3\mu\text{m}$, an initial ion distribution radius is $25\mu\text{m}$, and an initial transverse velocity from 0 to 300m/s uniformly and an initial longitudinal velocity of 1km/s .

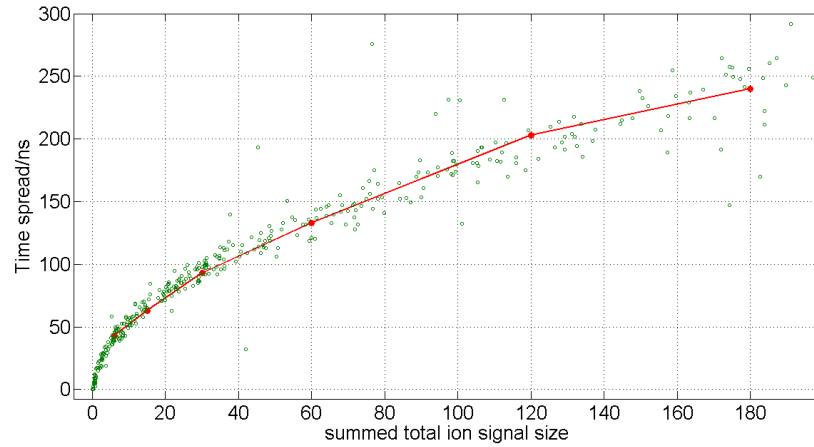


Figure 5.7 Simulation of BMIM+ in a 3 kV/cm external electric field. Green circles are experiment data. Red curve with dots is outcome of simulation. Reservoir thickness is $3\mu\text{m}$, initial ion distribution radius is $25\mu\text{m}$, birth transverse velocity is from 0 to 300m/s and birth longitudinal velocity is 1 km/s .

To calibrate the measured total ion signal to the simulation total ion count, we matched a broadened, symmetric, experimental peak shape to a 40 thousand ion simulation, as shown in Fig. 5.8. We compute a conversion factor as the ratio between integral of the chosen shot signal and 40 thousand. Figure 5.9 compares 4×10^5 ion count simulation peak with real data whose count is the same estimated from total signal multiplied by conversion factor. Current model predicts BMIM+ behavior under strong external electric field fairly well.

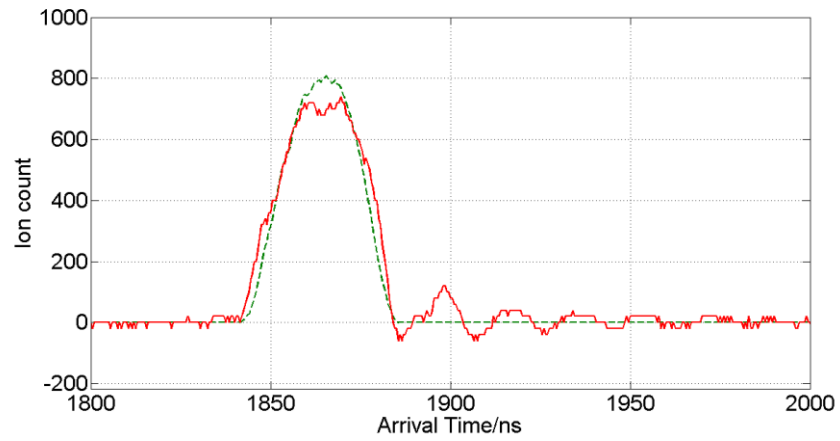


Figure 5.8 low ion count data (red) shot (total integral signal is 6) versus simulation outcome (green) with similar peak width (40 thousands ions). Conversion factor between ion counts and integral signal is determined as $20000/3$.

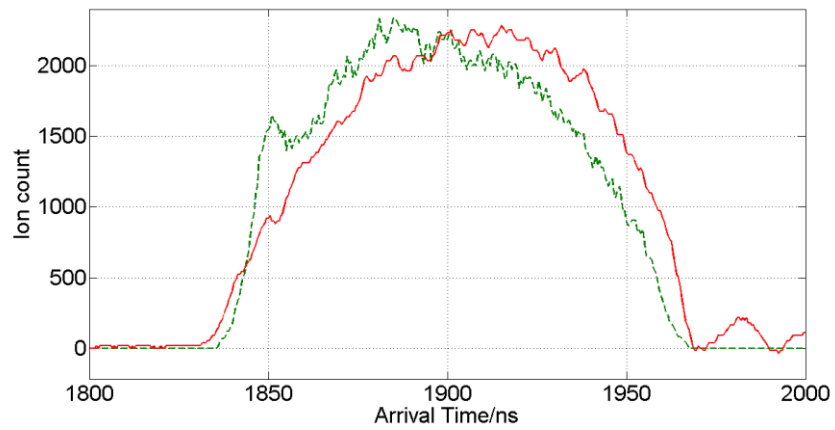


Figure 5.9 with conversion factor calculated by low ion count, high ion counts (0.4 million, green) simulation outcome has comparable peak width to high integral signal shot from experiment data (red).

Figure 5.10 shows a comparison of experimental data to a simulation of Chromium ions (mass is 52) with same model and parameters as for the BMIM+ (mass = 139) case. The experimental data closely matches the simulation, although there appears to be a systematic difference at low ions counts. We believe that the presence of other ion species, especially iron whose mass is close to chromium affects the peak shape of chromium. At higher ion counts, these effects are minimized.

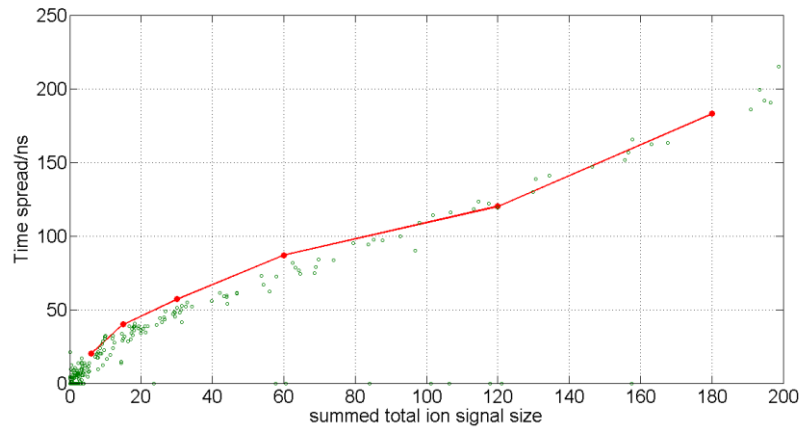


Figure 5.10 simulation outcome compared with Cr⁺ ions from experiment data. External field is 3kV/cm. Reservoir thickness is 3 μ m, initial ion distribution radius is 25 μ m, birth transverse velocity is from 0 to 300m/s and birth longitudinal velocity is 1km/s.

5.2.4 Simulation Parameters Discussion

There are three main parameters to describe our reservoir model: the reservoir radius, the launching field required to eject an ion from the reservoir, and the reservoir thickness. We chose the radius of the reservoir to be the same as the laser spot size; however, the laser spot is elliptical, rather than circular. Consequently, we have tested the reservoir model to see if it is sensitive to the initial shape. Our simulations show that the ions are more quickly ejected from the edges of the reservoir, where there is less shielding of the acceleration field, so an ellipse quickly devolves into a more circular shape. Figure 5.11 compares the arrival times of ions from elliptical and from circular initial

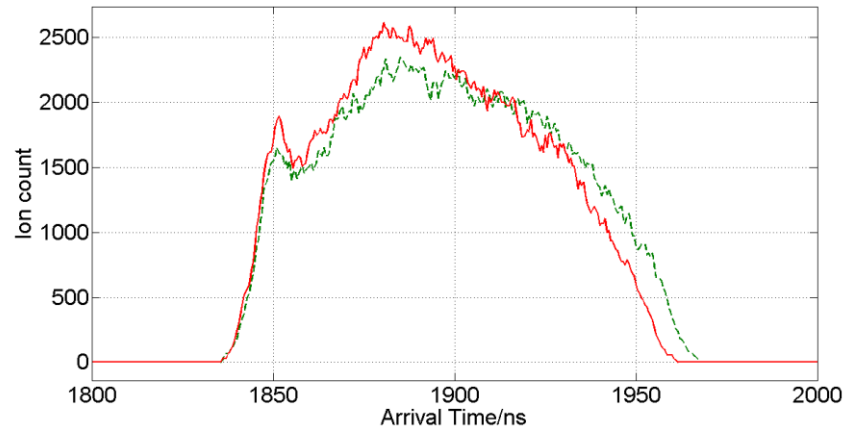


Figure 5.11 circular initial ion distribution (green) versus elliptical initial distribution (red). Final time distribution is independent of initial ion distribution shape under same charge density. Reservoir thickness is 3 μm , initial ion distribution is elliptical whose semi-major axis is 35 μm and semi-minor axis is 18 μm . Birth transverse velocity is from 0 to 300 m/s and birth longitudinal velocity is 1 km/s.

ion distributions with 2000 ion cells multiplied by 200 (for a total of 400,000 equivalent ions). The semi-major axis of the ellipse is 1.4 times larger than the radius of the circle while the semi-minor axis is 1.4 times smaller (keeping the area constant). For the same initial charge density, both spot shapes provide almost the same arrival time distribution. In the simulation, ions move out of the reservoir only when the average field in a region near the surface of the reservoir is above a threshold, which we call the launching field. As shown earlier, this serves to eliminate ion oscillations in the reservoir without requiring a full scale calculation of the electron motion. Figure 5.12 compares simulations of the arrival time distribution for 4 million BMIM⁺ ions at 3 kV/cm electric field using two different threshold ejection fields of 1%

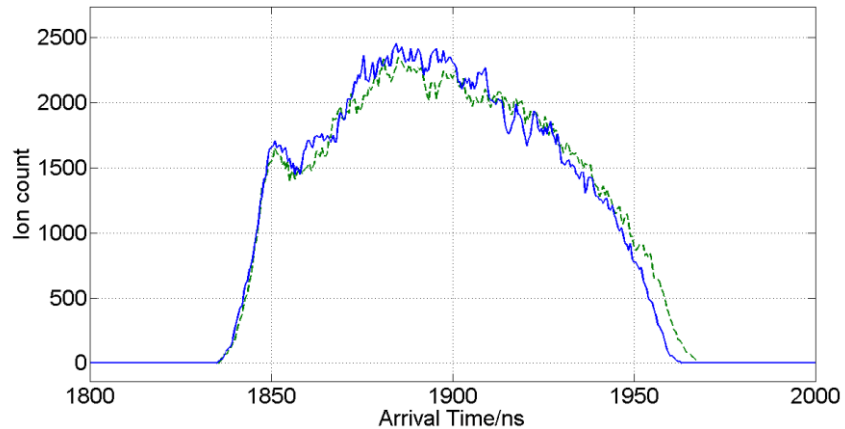


Figure 5.12 Launching field threshold comparison. Green distribution threshold is set at 5% of external electric field. Blue is set at 1% of external electric field. Both are 4 million BMIM⁺ case in 3kV/cm external electric field. Reservoir thickness is 3 μ m, initial ion distribution radius is 25 μ m, birth transverse velocity is from 0 to 300m/s and birth longitudinal velocity is 1km/s.

and 5% of the applied acceleration field. This change in the threshold field has almost no impact on the final time distributions.

Due to the complicated laser pulse shape, and the highly non-linear ionization process, the effective laser pulse length is another uncertainty in our experiment. Figure 5.13 compares time distributions with different effective length of laser pluses, i.e. 5 ns and 10 ns.

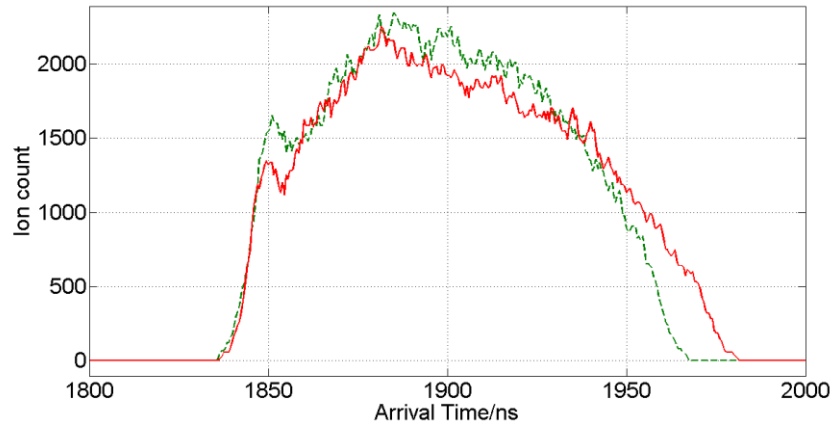


Figure 5.13 simulation outcomes with 5 ns (green) and 10 ns (red) wide laser pulse. Peak width variance is less than 10 percent. Reservoir thickness is 3 μm , initial ion distribution radius is 25 μm , birth transverse velocity is from 0 to 300 m/s and birth longitudinal velocity is 1 km/s.

Excluding laser pulse length variance, the difference is less than 10% which has no significant influence on simulation outcomes so that there is no need to be concerned with effective laser pulse length variance in our simulation.

The reservoir thickness is the most sensitive parameter for the simulation. In Figure 5.14, we compare simulations with different reservoir thicknesses for BMIM⁺ accelerated through fields of approximately 3 kV/cm. Peaks with the same total ion count become

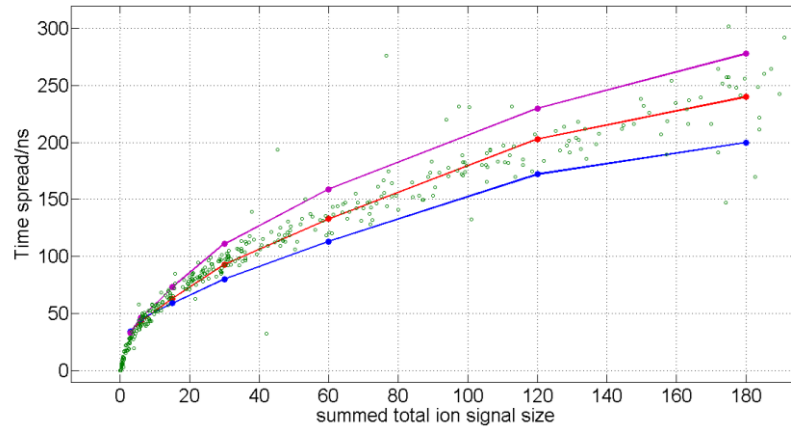


Figure 5.14 BMIM⁺ in strong field simulation with different reservoir thickness. Blue is outcome of 5 μm thick reservoir. Red is 3 μm and purple is 1 μm. Higher reservoir will narrow the peak width under the same quantity of ions.

narrower when the simulation uses a larger reservoir thickness.

The electrons always respond to an electric field quickly. After desorption with some initial energy, the electrons will move upwards until their velocity slows to zero and becomes negative. The returning electrons will build a sheath to shield the external electric field from penetrating into the neutral quasi-plasma near the target surface. We chose the maximum height the initial electrons could reach as our reservoir thickness choice. The cold electrons with 1 eV initial energy

will reach to about 3 μm in 3 kV/cm field, while electrons with the same 1eV energy will continue to 9 μm in a smaller 1 kV/cm. Figure 5.15 shows simulation results when an applied 1 kV/cm electric field is used in first 1 cm and 2 kV/cm field in next coming 1 cm which guarantee same 3 kV energy as in regular 3 kV/cm experiment setup with 9 μm thick reservoir. The simulation fits experiment data well from low to high ion production range for the weak field test.

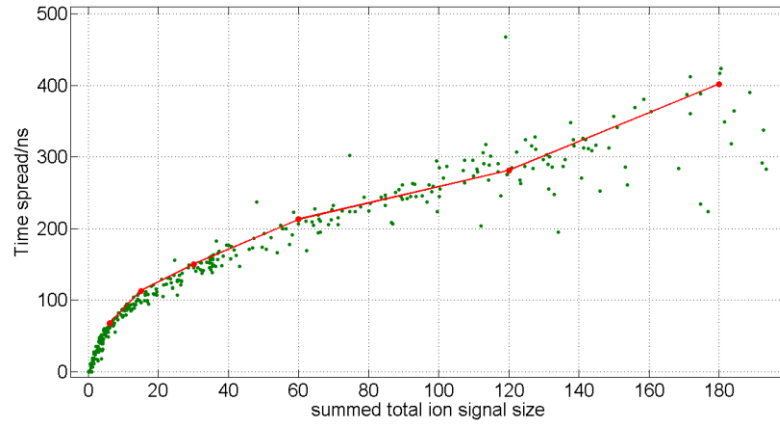


Figure 5.15 BMIM+ simulation in weak field, *i.e.* 1kV/cm throughout the first centimeter and 2 kV/cm in the second centimeter to maintain 3 keV as the total energy. The red curve was constructed using a 9 μm reservoir thickness. The initial ion distribution radius is 25 μm , initial transverse velocity has a random distribution from 0 to 300 m/s. The initial longitudinal velocity is 1 km/s.

5.2.5 Collection Efficiency Decrease after long flight

From our simulation of BMIM⁺ ions in a 3 kV/cm external electric field, we find that the electrostatic repulsion spreads the ion beam so that some of ions miss the detector when it is 50 cm from the source.

Figure 5.16 displays time distribution of 4×10^5 BMIM⁺ ions reaching the detector at 50 cm, after being accelerated through 3 kV. The red curve is the arrival time distribution of all the ions, whereas the blue curve

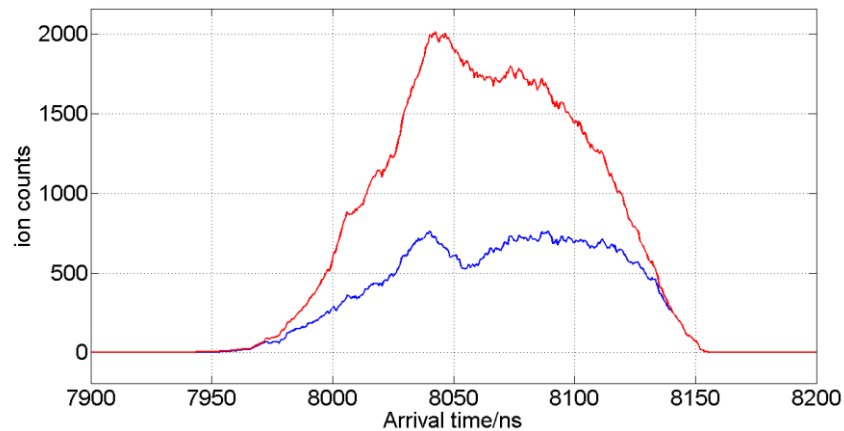


Figure 5.16 0.4 million BMIM⁺ time distribution at 50 cm detector with 3 kV/cm electric field. Red is distribution collecting all ions. Blue only collects ions within detector dimension at 50 cm.

shows the arrival times of only those ions within a 1.25 cm radius of the center of the detector. The active region of the detector is a 1.25 cm radius circle.

Figure 5.16 shows the collection efficiency to be 44% in this case.

Figure 5.17 compares the reduced collection simulation to the data from a single laser shot, whose total ion production we estimate to be close to 4×10^5 .

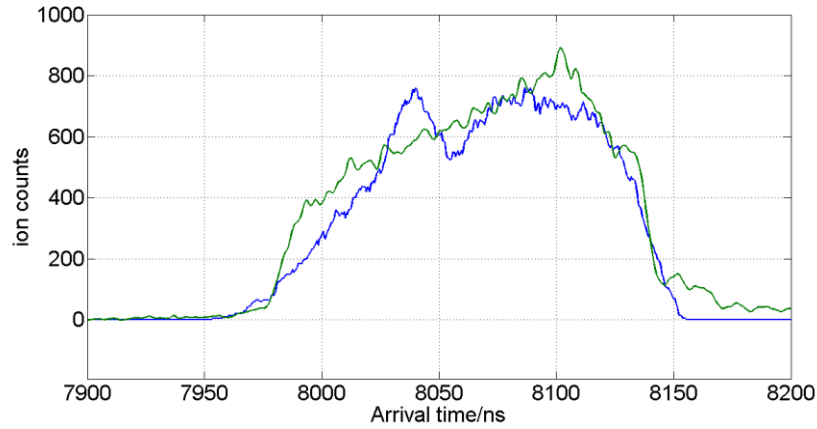


Figure 5.17 Time distribution of simulated 0.4 million BMIM+ ions collected (Blue) by detector compares to a similar ion production shot in experiment data with the detector at 50 cm from the ion source (Green).

In Fig. 5.17, the peaks widths are equivalent and both show a sharp cut-off edge on the late arrival side. Similar simulation runs with different ion productions from 40 thousand to 1.2 million show similar reductions in the collection efficiency. Figure 5.18 shows good agreement between our collected data and our simulations for both the near and far detector positions, as long as the decreased collection effects are included for the far detector.

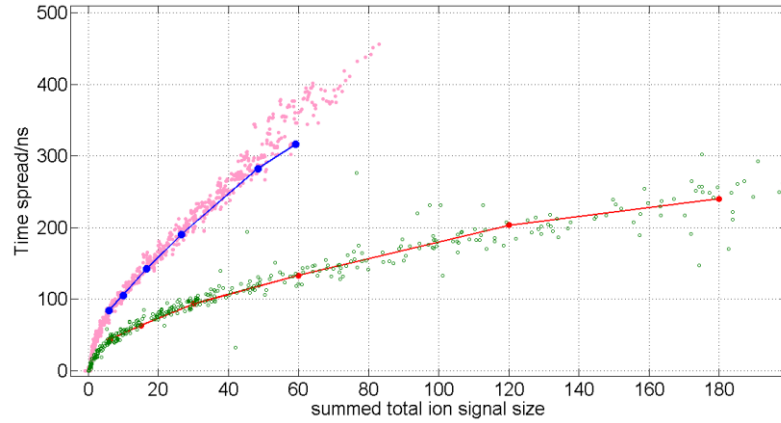


Figure 5.18 Time spread of BMIM⁺ ion at 3kV/cm source electric field. Green dots are experiment data of detector at 10cm. Pink are data of detector at 50cm. Red and blue curves are simulation outcome collecting ions within detector radius 1.25cm at 10cm and 50cm far from ion source.

5.4 Azimuthally symmetric slices model

The Vlasov equation describes the time development of the distribution function of a collisionless plasma composed of charged particles interacting via the Coulomb force. In our model, the Vlasov equation would properly account for the cell movement, but also for the movement of ions between cells due to a velocity gradient. To test this we developed a slice model that reduced the volume, and replicated that volume with azimuthally symmetric slices that filled the space. In this case, we could reduce the number of ions in a cell, but make the

slice volume large enough that the exchange of ions between slices should be minimal. We then used a GPU parallel computing technique to solve for the motion of the less dense slices to confirm the accuracy of our mean field model that used a larger number of ions per cell.

$$\frac{\partial f}{\partial t} + \vec{v} \cdot \nabla f + \frac{q}{m} (\vec{E} + \vec{v} \times \vec{B}) \cdot \nabla_v f = 0 \quad 5.1$$

5.4.1 GPU parallel computing

Graphics Processing Units (GPUs) were introduced to accelerate graphics rendering. Although they were powerful, and designed to be used in parallel computing, GPU programming was complicated, requiring the expertise of GPU architecture. The introduction of higher level libraries such as NVIDIA Compute Unified Device Architecture (CUDA) in 2006 and OpenCL in 2008 simplified software applications and further promoted wide usage of GPUs. In recent years, low cost and high performance GPUs have become a credible tool to accelerate scientific computational problems. A typical GPU will include hundreds of cores, unlike a conventional CPU that includes only a few cores. MATLAB provides a parallel computing toolbox to enable MATLAB code to run on a GPU with only simple code changes to save calculation time and achieve other models.

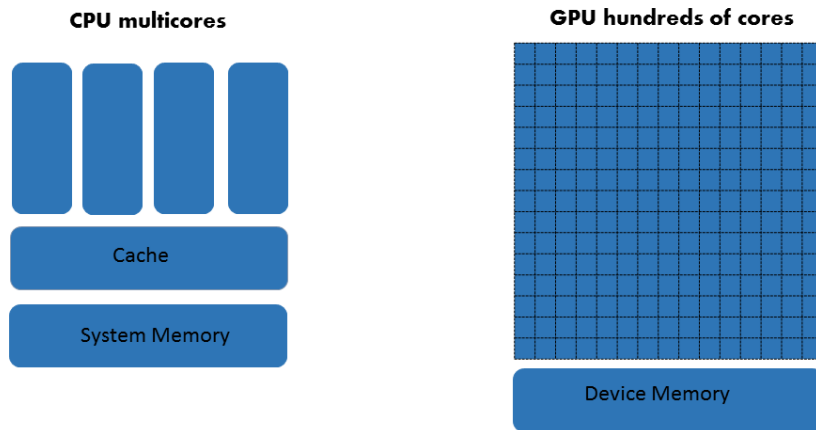


Figure 5.19 CPU and GPU architecture comparison

5.4.2 Slices Model

The slices model and the mean field model only differ in the volume occupied by the cells and by the number of ions in each cell. The slices model uniformly distributes hundreds of ions in a small circular sector whose central angle will be less than 10 degree and then replicates that sector to build a full circular distribution. Using the overall azimuthal symmetry, the slice model simulation ignores ion movement in the azimuthal direction and only tracks ion movement in the radial and height directions for a single sector. Each ion in the sector feels the force of the other ions in the sector, and the force from the replicated versions of all the ions (including itself) in the other sectors.

We still use a multiplier to put several ions in a cell when using the slices model to keep the computational time to less than a few hours with NVIDIA GeForce GT 640 graphic card. Figure 5.20 shows a simulation outcome of 400 thousand BMIM⁺ ions in the 3kV/cm field where the mean field model uses 2000 ion cells with 200 ions in each cell and the slices model uses 400 ion cells with 50 slices and only 20

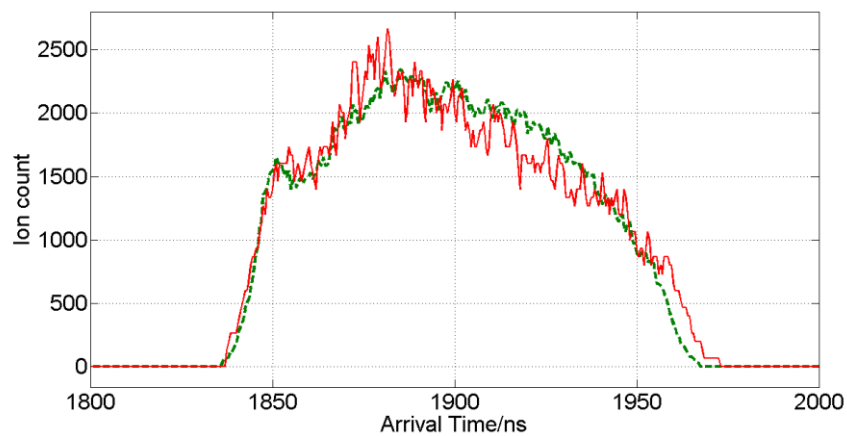


Figure 5.20 Comparing 0.4 million ion simulations using the mean field model (green) and the slice model (red). Each cell in the slices model contains only one tenth of the 200 ions in the mean field model. Yet, the distributions are nearly identical.

ions in each cell.

Figure 5.21 shows that the slice model results (blue curve) is very close to mean field model, having a difference in time spread of less than 5% at high ion counts. Although the number of ions in a cell is much smaller using the slice model, the similar results show the

exchange of ions between cells is not an important factor in either of these simulations.

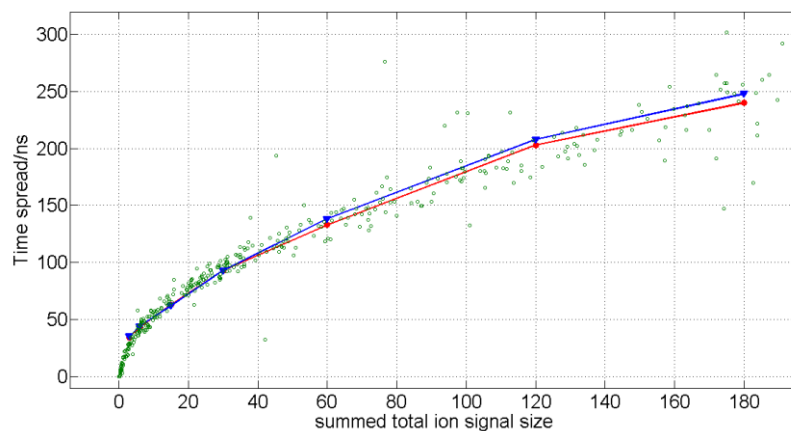


Figure 5.21 Ion reservoir model (red) compared with slices model with GPUs parallel computing technique. Simulation runs with BMIM⁺ ions in 3kV/cm external electric field.

Chapter 6

Conclusion

This work demonstrates that the primary cause of the mass resolution degradation with increasing ion signal is that the ionic space charge delays the ejection of ions into the acceleration region. This work uses a simple and flexible apparatus that avoids the advanced techniques used to enhance MALDI resolution and uses a self-healing liquid matrix to improve the surface stability. This work illustrates this delayed ionic ejection by showing that the additional time broadening of a particular ionic arrival time does not increase when the detector is moved to a farther position, increasing the net arrival time. This work also provides a series of simulations documenting how image charges and space charge can eliminate the acceleration field for times as long as hundreds of nanoseconds.

6.1 Resolution degradation

With relatively low laser power, our apparatus generates spectra with resolution as large as 150 in the low mass range, even though our apparatus has a short free flight length, and a low (1-3 kV/cm) extraction field. For high laser powers, we observe that the width of the arrival time peak of BMIM⁺ ions increases linearly with the total ionic signal, thereby degrading the peak resolution. We have verified that this increase in the width of the arrival time distribution does not depend on the net travel time, and so it cannot be due to an increase in the velocity spread of the ions, but must instead be due to an increase in the ejection time of the ions. We have simulated the ion-ion interaction during the flight time, and the cancelation of the acceleration field due to the space charge of the ions that have already been ejected. We find that the ejection time decreases with increasing acceleration field. This suggest that the delayed ion extraction method may decrease the mass resolution at high ionic signals, making it counter-productive.

Simulation provides an explanation of full peak width variance with same ion production from different location detectors. A detector located at 50 cm from the source will miss almost half of all the ions but will collect all ions when located near the desorption source.

The peak resolution only relies on the initial electric field instead of energy gained from acceleration space illustrating that the degradation in our TOF-MS is caused by different initial launch times from the source region while the velocity spread in the free flight tube contributes little to eventual time spread in our spectra.

6.2 Space charge

This work shows that the peak resolution degradation arises from a delay in the ejection of ions into the acceleration field, which is equivalent to increasing the laser pulse length. The first ions ejected from the source plasma build up a space charge cloud shielding, and eventually cancelling, the accelerating electric field. As those ions move away, the electric field continues to extract ions from the source plasma, again cancelling the electric field. This process continues until all of the ions have been extracted (or have recombined), prolonging the time of the initial pulse of ions. We have demonstrated this by showing that fewer ions create this space charge to prolong the ejection process when the extraction field is weaker. Our simulations of this space charge effect model fits experiment well with a variety of different experimental parameters.

Delayed ion ejection is a very different process than one that increases the initial velocity (or energy) spread. When the increased width in the arrival distribution is due to delayed ion ejection, the width will remain the same, even for different flight tube lengths. If it had been due to an increase in the velocity spread, then the increased width would be proportional to the arrival time, *i.e.* the flight tube length. We observe the increased width to be independent of the arrival time for lengths of 10 cm and 25 cm. For our longest flight tube length (50 cm), we believe that we are only detecting a fraction of the large signal ions, based on our simulation's prediction that the ion beam has spread to a size larger than our detector. Our simulations show that this will reduce the ion count by as much as half. When we correct the total ion count of the 50 cm data for this effect, the width increase is again nearly independent of flight tube length.

BIBLIOGRAPHY

- [1] W. E. Stephens, *Bull. Am. Phys. Soc.* **21**, No. 2, p. 22 (1946)
- [2] A. E. Cameron and D. F. Eggers, Jr., *Rev. Sci. Instr.* **19**, 605 (1948)
- [3] M. Wolff and W. E. Stephens, *Rev. Sci. Instrum.* **24**, 616 (1953)
- [4] M. Karas, D. Bachmann and F. Hillenkamp, *Anal. Chem.* **57**, 2935 (1985)
- [5] K. Tanaka, H. Waki, Y. Ido, *et al. Rapid Commun Mass Spectrum*, **2**, 151 (1988)
- [6] "Cancer Facts & Figures 2015" American Cancer Society
- [7] P. James, *Quarterly reviews of biophysics* **30** (4), 279 (1997)
- [8] Z. Xiao, D. Prieto, T. Conrads, T. Veenstra and H. Issaq, *Molecular and Cellular Endocrinology* **230**, 95 (2005)
- [9] Cho, William CS., *Genomics, Proteomics & Bioinformatics* **5.2**, 77 (2007)
- [10] Xiao, Zhen, *et al, Molecular and cellular endocrinology* **230.1**, 95 (2005)
- [11] Yates, R. John, Cristian I. Ruse, and A. Nakorchevsky, *Annual review of biomedical engineering* **11**, 49 (2009)
- [12] Li, Jinong, *et al, Clinical chemistry* **48.8**, 1296 (2002)

- [13] Cramer, Daniel W., et al, *Cancer prevention research* **4.3**, 365 (2011)
- [14] Zhu, Claire S., et al, *Cancer Prevention Research* **4.3**, 375 (2011)
- [15] Westman-Brinkmalm, Ann, and Gunnar Brinkmalm, *Mass Spectrometry: Instrumentation, Interpretation, and Applications* (2008): 15-87.
- [16] Yates, John R., Cristian I. Ruse, and A. Nakorchevsky, *Annual review of biomedical engineering* **11**, 49 (2009)
- [17] Gatlin-Bunai, Christine L., et al, *Journal of proteome research* **6.11**, 4517 (2007)
- [18] M. Zabet-Moghaddam, E. Heinzle and A. Tholey, *Rapid Commun. Mass Spectrom.* **18**, 141 (2004)
- [19] M. Zabet-Moghaddam, E. Heinzle, M. Lasaosa, A. Tholey, *Anal. Bioanal. Chem.* **384**, 215 (2006).
- [20] A. Tholey, M. Zabet-Moghaddam and E. Heinzle, *Anal. Chem.* **78**, 291 (2006)
- [21] A. Tholey, E. Heinzle, *Anal. Bioanal. Chem.* **386**, 24 (2006)
- [22] J. Fenn, M. Mann, C. Meng, S. Wong, C. Whitehouse, *Science* **246**, 64 (1989)
- [23] C. Ho, M. Chan, R. Cheung, L. Law, L. Lit, K. Ng, M. Suen, H. Tai, *Clin Biochem Rev* **24**, 3 (2003)
- [24] P. Kebarle, U. Verkerk, *Mass Spectrometry Rev* **28**, 898 (2009)
- [25] R. Zenobi, R. Knochenmuss, *Mass Spectrometry Reviews* **17**, 337 (1998)
- [26] R. Cotter, *Time-of-Flight Mass Spectrometry: Instrumentation and Applications in Biological Research* (American Chemical Society, Washington, DC, p.113, 1997)

- [27] I. Fournier, J. Tabet and G. Bolbach, *International Journal of Mass Spectrometry* **219**, 515 (2002)
- [28] I. Chernushevich, A. Lodoba, B. Thomson, *Journal of Mass Spectrometry* **36** (8): 849 (2001)
- [29] D. Douglas, A. Frank, D. Mao, *Mass Spectrometry Rev.* **24** (1): 1 (2005)
- [30] Q. Hu, R. Noll, H. Li, A. Makarov, M. Hardman, R. Cooks *Journal of Mass Spectrometry* **40** (4): 430 (1997)
- [31] Sarah Houlton, *Manufacturing Chemist*, June 2004
- [32] Z. Alfassi, R. Huie, B. Milmann, P. Neta, *Anal. Bioanal. Chem* **377**, 159 (2003)
- [33] T. Yan, S. Li, W. Jiang, X. Gao, B. Xiang and G. Voth, *J. Phys. Chem. B* **110**, 1800 (2006)
- [34] R. Lynden-Bell, M. Del Popolo, *Phys. Chem.* **8**, 949 (2006)
- [35] R. Brown, J. Lennon, *Anal. Chem.* **67**, 1998 (1995)
- [36] B. Mamyrin, V. Karataev, D. Shmikk and V. Zagulin, *Sov. Phys. JETP* **37**, 45 (1973)
- [37] J. Dawson, *Rev. Mod. Phys.* **55**, 403 (1983)
- [38] J.P. Boris, *Proceedings of the Fourth Conference on the Numerical Simulation of Plasmas*, **Nov. 2-3**, 3 1970
- [39] C.K. Birdsall, A.B.Langdon, *Plasma Physics via Computer Simulation*, Taylor & Francis, 2004

VITA

Guangzhi Qu was born on October 23, 1984 and grew up in Dalian, Liaoning China. After graduating from Dalian Yuming High School in 2003, he enrolled at University of Science and Technology of China in Hefei, Anhui China. He graduated with Bachelor of Science in Physics in 2007. In fall of 2007 he enrolled in PhD program at the College of William and Mary in Williamsburg, Virginia.